Tin-pest problem as a test of density functionals using high-throughput calculations

Michael J. Mehl,[1,*] Mateo Ronquillo,[2] David Hicks,[1] Marco Esters,[1] Corey Oses,[1] Rico Friedrich,[1] Andriy Smolyanyuk,[1] Eric Gossett,[1] Daniel Finkenstadt,[3] and Stefano Curtarolo[1,†]

[1]*Center for Autonomous Materials Design, Duke University, Durham, North Carolina 27708, USA*

[2]*U. S. Nuclear Power School, Goose Creek, South Carolina 29445, USA*

[3]*Physics Department, U.S. Naval Academy, Annapolis, Maryland 21402, USA*

(Received 14 October 2020; revised 9 July 2021; accepted 6 August 2021; published 30 August 2021)

At ambient pressure tin transforms from its ground state, the semimetal α-Sn (diamond structure), to metallic β-Sn at 13 °C (286 K). There may be a further transition to a simple hexagonal phase, γ-Sn, above 450 K. These relatively low transition temperatures are due to the small energy differences between the structures, $\approx$20 meV/atom between α- and β-Sn, which makes tin an exceptionally sensitive test of the accuracy of density functionals and computational methods used in calculating electronic and vibrational energy, including zero-point energy. Here we use the high-throughput automatic-flow (AFLOW) method to study the energetics of tin in multiple structures using a variety of density functionals and examine the vibrational contributions to the free energy with the AFLOW Automatic Phonon Library (APL). We look at the successes and deficiencies of each functional. We also discuss the necessity of testing high-throughput calculations for convergence of systems with small energy differences.

DOI: 10.1103/PhysRevMaterials.5.083608

I. INTRODUCTION

It is said that the failure of Napoleon's invasion of Russia was caused, in part, by the disintegration of his troops' tin buttons during the cold winter of 1812–13 [1]. Tin has also been blamed for the failure of the 1910–13 Scott Expedition, as their caches of kerosene evaporated, supposedly from a failure of the tin solder in the tanks [2].

While both of these stories are apocryphal (indeed, the Grande Armée's buttons were most likely brass, not pure tin), tin failure has been seen in nature. Fritzsche [3] reported that in the Russian winter of 1687–1688 a stockpile of tin transformed into rods and powder. In the winter of 1867–1868 tin pipes stored in the cold of St. Petersburg also met the same fate. Shaum [4] also collected evidence of the phase transition. In particular, he reported a sample of "white" tin which had been partially converted into "gray" tin could be transformed back to white tin upon heating. The low temperature gray tin structure was eventually designated α-Sn, while the room temperature structure is known as β-Sn. Less interesting to historians, but of technological importance to modern society, lead-free tin solders have also failed by the same mechanism [5–7].

This legendary and actual degradation of element 50 is known as *tin-pest* [8]. Below 286 K metallic β-Sn transforms into brittle, semimetallic, α-Sn with a 20% increase in volume [9,10]. This transformation is slow but dramatic [11] and leads to extensive damage to the tin sample.

In addition to the well-known white and gray phases, there is some evidence that tin can transform from β-Sn to γ-Sn at 450 K [12]. This phase is said to be a slight orthorhombic distortion of the simple hexagonal lattice, a structure not observed at ambient pressure in any other element. The simple hexagonal structure has been observed in samples of tin alloyed with either cadmium, indium, lead, or mercury [13–15], as well as tin-free alloys such as $In_{0.45}Bi_{0.55}$ [16].

These relatively low temperature phase transitions imply that the equilibrium structures of the three phases are very close in energy. The static lattice energy difference between α- and β-Sn has not been directly determined by experiment, but it is estimated to be in the range of 10–40 meV/atom [17,18]. This makes the prediction of the α-Sn $\leftrightarrow$ β-Sn transition difficult for density functional (DFT) calculations, which may not achieve the required accuracy [17,19–22]. Tin is therefore an ideal test case for assessing the accuracy of various density functionals.

Since the tin phase transitions are thermal we can only predict the transition temperature by finding the vibrational free energy of the tin phases from their phonon frequencies, which will be volume dependent. This, in turn, requires many calculations involving large supercells and is best handled by high-throughput methods. High-throughput methods are generally optimized for speed, so this introduces another source of error: The basis set and k-point mesh sizes set by default in these programs might not be accurate enough to find the correct ordering of phases. Thorough testing of the predictive capability of different functionals also requires testing of convergence criteria in the programs that evaluate DFT energies.

Here we determine the free energy of the three tin phases for several DFTs. First we determine the static lattice energy at multiple volumes in a variety of crystal structures, looking

*michael.mehl@duke.edu
†stefano@duke.edu

for the static ground state of tin; next we compute the phonon spectra for the α-, β-, and γ-Sn phases at each volume; finally we evaluate the free energy for each phase as a function of temperature.

The largest part of this work will be determining phonon frequencies, which we do by extracting the harmonic interatomic force constants (IFC) from first-principles calculations of supercells involving 125–180 atoms. We do this using the high-throughput AFLOW (automatic FLOW) platform [23–28] and its Automatic Phonon Library (APL) [23,29] to set up the supercells, run the first-principles calculations to determine the atomic forces, and interpret the results. AFLOW in turn uses the Vienna *Ab initio* Simulation Package (VASP) to perform its first-principles calculations [30–33].

Our strategy is to use AFLOW and VASP to look at possible crystal structures for elemental tin using the local, generalized-gradient, and meta-GGA density functionals available in VASP. While the hoped-for result is that all functionals give us the same result, it is known that different functionals can predict quite different ground state structures [34]. Here a successful functional will predict that α-Sn is the ground state of tin, the β-Sn phase is close enough in energy so that a room-temperature thermal phase transition is possible, and the γ-Sn phase (if it exists) will be just above β-Sn. In cases where this is true, we can then compute the phonon spectra of these phases as a function of volume, use this to find the free energy as a function of temperature within the quasiharmonic approximation (QHA) [35], and determine the functional's prediction of the transition temperature.

Since the energy differences involved here are so small, we must check that the default settings for the VASP calculations used by AFLOW are accurate. We therefore study the effect of changing basis set size and k-point meshes on the energy differences between the phases.

The paper is organized as follows: Section II describes the crystal structures investigated in this paper, including the many ways the structures are referred to in the literature. Section III gives a brief description of the density functionals used in this study, with theoretical and computational details provided in Sec. IV. Section V tests the default convergence settings in AFLOW by comparing those calculations with calculations involving larger sets of basis functions and k points. Section VI looks at the static lattice (no phonon) energy-volume behavior of tin using the LDA, GGA, and meta-GGA density functionals available in VASP. Free energy calculations require calculation of the phonon spectra of each phase as a function of volume. We discuss the convergence of these calculations with supercell size and k-point mesh in Sec. VII. Section VIII C considers the thermal properties of the α-, β-, and γ-Sn phases, including predictions of phase transition temperatures for those functionals which predict the correct ordering of the phases. Section IX estimates the previously neglected thermal contribution of the electrons to the free energy and discusses possible changes to the phase transition temperatures. Finally, we discuss the results in Sec. X.

II. CRYSTAL STRUCTURES

We determined the static lattice energy/volume behavior for tin using the crystal structures observed in the group-IV elements, as well as some close-packed and nearly close-packed elemental structures typical of metals. Some of the many notations for these structures are summarized here:

(i) The common names of the structures (e.g., fcc, bcc, diamond or α-Sn, β-Sn, simple hexagonal or γ-Sn, etc.). In most cases we will refer to the structures using this notation.

(ii) *Strukturbericht* designations serve as a shorthand designation of the structures. We use the designations provided in the original *Strukturbericht* volumes [39] and the extensions proposed by Smithells [40]. Unfortunately Lonsdaleite [41], the hexagonal diamond structure, has no *Strukturbericht* entry. We will primarily use the *Strukturbericht* labels in graphs to avoid clutter, abbreviating Lonsdaleite as "Lons."

(iii) For high-throughput calculations it is helpful to have a label which allows both the user and the computational algorithm to compactly specify the structure. Since we are using AFLOW we use the AFLOW prototype label [36], which uniquely specifies the stoichiometry, space group, and Wyckoff positions of the structure. Thus the diamond ($A4$, α-Sn) structure is A_cF8_227_a, as it has one type of atom (A), a face-centered cubic primitive cell with eight atoms in the conventional cell (Pearson symbol cF8), and is in space group #227 ($Fd\bar{3}m$) with the atoms at the (8a) Wyckoff position.

More details about the structures, including the above information and a full description of the primitive lattice vectors and basis vectors, can be found in the Library of Crystallographic Prototypes [36–38,42]. The Library also allows the user to generate structure files for use as input in a wide variety of electronic structure codes, including the POSCAR files for these AFLOW/VASP calculations.

Table I describes all of the structures used here, including the common name, *Strukturbericht* label, space group, and AFLOW prototype. The online version also provides a link to the corresponding entry in the Library of Crystallographic Prototypes.

The face-centered cubic ($A1$), body-centered cubic ($A2$), and both body-centered tetragonal structures ($A6$, A_a) can all be derived from one another by stretching or compressing the primitive cell along the (001) direction, with the $A6$ structure having a c/a ratio close to the $A1$ structure, and A_a near $A2$.

The structures of most interest in this work are α-Sn (diamond structure, gray tin, or $A4$), β-Sn (white tin or $A5$) and simple hexagonal γ-Sn (A_f) structures. These are shown in Fig. 1. The β-Sn structure can be obtained from α-Sn by compressing along the (001) axis of the diamond crystal.

A. The γ-Sn structure

While the α- and β-Sn structures are well known, the γ-Sn structure is not. Smithells [40], apparently referencing Raynor and Lee [43], used $HgSn_{10}$ as the prototype for *Strukturbericht* designation A_f with hexagonal space group $P6/mmm$ #191 and one atom per unit cell located at the (1a) Wyckoff position. This can only be achieved if the mercury and tin atoms are randomly placed on the (1a) site. Alloys of tin with 5–20% cadmium, indium, lead, and mercury also exhibit this structure, which is generally referred to as the γ phase [13–15]. Parthé *et al.* [16] also list $In_{0.45}Bi_{0.55}$ under the A_f designation.

Though it is not the ground state of any element, the simple hexagonal phase (γ-Sn) is observed at high pressures

TABLE I. The elemental crystal structures investigated in this paper. As Lonsdaleite does not have a *Strukturbericht* designation we abbreviate it as "Lons." In the electronic versions of this paper the AFLOW prototype column is linked to the appropriate page in the Library of Crystallographic Prototypes [36–38].

Common name	*Strukturbericht*	Atoms/cell	Space group	AFLOW prototype
fcc (face-centered cubic)	$A1$	1	$Fm\bar{3}m$ #225	A_cF4_225_a
bcc (body-centered cubic)	$A2$	1	$Im\bar{3}m$ #229	A_cI2_229_a
hcp (hexagonal close-packed)	$A3$	2	$P6_3/mmc$ #194	A_hP2_194_c
diamond (α-Sn)	$A4$	2	$Fd\bar{3}m$ #227	A_cF8_227_a
β-Sn	$A5$	2	$I4_1/amd$ #141	A_tI4_141_a
In (body-centered tetragonal)	$A6$	1	$I4/mmm$ #139	A_tI2_139_a.In
α-Pr (body-centered tetragonal)	A_a	1	$I4/mmm$ #139	A_tI2_139_a.alpha-Pa
γ-Sn (simple hexagonal)	A_f	1	$P6/mmm$ #191	A_hP1_191_a
sc (simple cubic)	A_h	1	$Pm\bar{3}m$ #221	A_cP1_221_a
Lonsdaleite (hexagonal diamond)	Lons.	4	$P6_3/mmc$ #194	A_hP4_194_f

in silicon [44] and germanium [45]. Needs and Martin [44] found that the simplest possible transition between β-Sn and γ-Sn is described by distorting either of the phases into a body-centered orthorhombic crystal, space group *Imma* #74, with the atoms at the (4e) Wyckoff position. This path can be described using a body-centered orthorhombic unit cell, space group *Imma*, with atoms occupying the (4e) Wyckoff positions, locating the atoms at

$$\vec{b}_{\pm} = \pm\left(\tfrac{1}{4}\, b\,\hat{y} + z\, c\,\hat{z}\right). \tag{1}$$

When $a = b$ and $z = 1/8$ this becomes the β-Sn structure. One can change β-Sn into α-Sn simply by moving along the Bain path [46] and setting $c = \sqrt{2}a$. The γ-Sn structure is found when $z = 1/4$, $a = 2c_{\rm hex}$, $b = \sqrt{3}a_{\rm hex}$, and $c = a_{\rm hex}$, where $a_{\rm hex}$ and $c_{\rm hex}$ are the lattice constants of the hexagonal structure. Note that in this case the primitive cell (1) contains two of the hexagonal primitive cells. This gives us a simple relationship between the α-, β-, and γ-Sn structures.

An elemental γ-Sn phase, occurring above 435 K, was apparently described around 1960, "but it is no longer mentioned [in] textbooks" [12]. In 1985 Kubiak [12] found that a structure he called the γ phase appeared after heating single crystal β-Sn in air at 450 K for one week. He described this structure as having space group *Cmmm* #65, with two atoms in the conventional orthorhombic cell located on the (2a) Wyckoff position and lattice parameters (a, b, c) =(5.8308 Å, 3.181 Å, 2.9154 Å). This structure is extremely close to simple hexagonal A_f, and when we run electronic structure calculations starting with Kubiak's γ-Sn structure it always relaxes to the simple hexagonal A_f structure. Given this we will only consider the hexagonal structure in our calculations below and refer to it as both γ-Sn and A_f.

We should note that this γ-Sn phase is not the structure described by Donohue [9]. That structure, also known as Sn-II, is a high pressure tetragonal structure which we do not consider here.

Wehinger *et al.* [47] did a first-principles study of hexagonal γ-Sn using the LDA functional. They found that it was energetically similar to β-Sn. They did not address its thermal behavior, nor did they discuss the relationship between β- and γ-Sn and the ground state α-Sn structure.

The orthorhombic elemental γ-Sn phase also can be stabilized in tin nanoparticles and nanowires [48]. We will not address this work here.

III. DENSITY FUNCTIONALS USED TO STUDY TIN

In our study of the tungsten-nitrogen system [34] we found that the predicted ground state structure of a compound can change with the choice of density functional. Given the small energy difference between tin phases it is quite possible that different functionals will give different ground state structures. In this section we describe the density functionals we used in this study. All are available in VASP.

(i) The local density approximation (LDA) [49–51], which determines the Kohn-Sham potential [52] at a given point in space using only the charge density at that point. It is well known that this functional underestimates equilibrium lattice volumes.

(ii) Generalized-gradient approximation (GGA) functionals, where the Kohn-Sham potential depends on the local charge density and its local gradient. These include

(1) Perdew-Burke-Ernzerhof (PBE) [53], perhaps the most widely used GGA. This generally overestimates equilibrium lattice volumes.

(2) Perdew-Burke-Ernzerhof revised for solids (PBEsol) [54], a modification of PBE optimized for solids rather than atoms.

(3) Armiento-Mattsson (AM05) [55], designed to describe surfaces, but which has proved to be very accurate for solids [56].

(iii) Meta-GGA functionals, which depend on the orbital kinetic energy density as well as the charge density and its gradient. VASP provides

(1) Tao-Perdew-Staroverov-Scuseria (TPSS) [57], designed to be correct for one- and two-electron systems and systems with slowly varying charge densities.

(2) "Revised" TPSS (revTPSS) [58], which includes the second-order gradient expansion for exchange.

(3) "Made-simple" functionals (MS0, MS1, MS2) [59,60], which have empirical parameters.

(4) M06-L [61], optimized for main-group and transition metal chemistry.

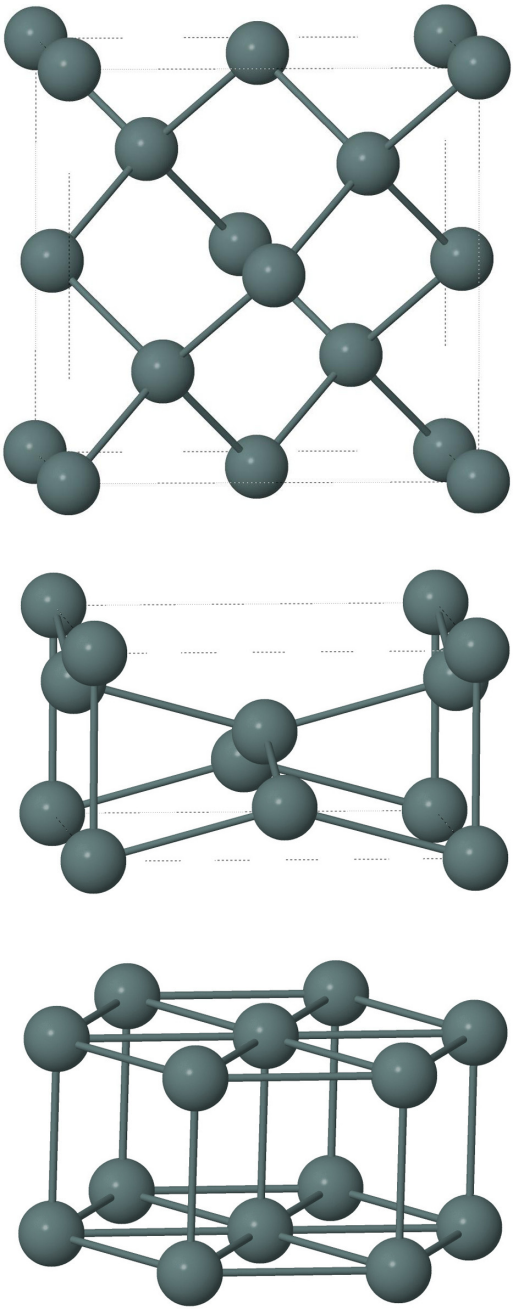

FIG. 1. The three low-energy structures of tin, drawn approximately to scale. Top: α-Sn, *Strukturbericht* $A4$ (gray tin, diamond structure), AFLOW Designation A_cF8_227_a. Middle: β-Sn, *Strukturbericht* $A5$ (white tin), AFLOW Designation A_tI4_141_a. Bottom: simple hexagonal γ-Sn, *Strukturbericht*A_f, AFLOW Designation A_hP1_191_a. The conventional cells are shown for the cubic α-Sn and tetragonal β-Sn. The γ-Sn figure contains three primitive cells to show the hexagonal structure.

(5) "Strongly constrained and appropriately normed" (SCAN) [62], which satisfies all known constraints on the exact density functional with no adjustable parameters. Since the SCAN functional properly describes both covalent and metallic bonding in silicon [63], it may be able to describe similar behavior in tin.

All of the meta-GGA functionals except SCAN give similar results for the static energies for the structures in Table I. Since a metaGGA calculation is more time consuming than LDA or standard GGA we will use revTPSS as the reference functional for these calculations.

The accuracy of these functionals has been tested with a variety of datasets [56,64,65], but to our knowledge there is no systematic test of the ability of density functional theory to describe the tin phase transition. Several papers [17–22] have discussed the α-β transition, and Ivanov and coworkers [14,15] have looked at the γ-Sn phase. No one, however, has looked at the relationship between all three phases, nor has there been any work discussing the differences in the predictions made by different density functionals.

IV. THEORY AND COMPUTATIONAL DETAILS

All calculations were performed using the high-throughput AFLOW (automatic FLOW) [23–25] framework. The first-principles calculations were done using the Vienna *ab initio* simulation package (VASP), version 5.4.4 [30–33], with VASP POTCAR files generated with the projector augmented-wave (PAW) method [66,67]. Calculations with the Perdew-Burke-Ernzerhof (PBE) functional [53] used the VASP s^2p^2 "Sn" PBE POTCAR (dated 08Apr2002). Local density approximation (LDA) and the other GGA functionals used the corresponding LDA POTCAR (03Oct2001), with the appropriate choice of the GGA or METAGGA tag in the INCAR file. Meta-GGA functional calculations require kinetic energy information only available in POTCARs available starting with VASP 5.4, so for those functionals we used the s^2p^2 LDA POTCAR (also dated 03Oct2001). In general we used the AFLOW defaults for energy cutoffs (1.4 times the value of ENMAX given in the VASP POTCAR file) and Γ-centered k-point meshes, with the exceptions noted below.

Electronic densities of states (eDOS) were computed by VASP using the eigenvalues determined in the self-consistent energy runs. We did not do a separate tetrahedron method calculation, as we only want to show general behavior of the eDOS.

Phonon spectra, vibrational free energy, and the thermal expansion of α-, β-, and γ-Sn were found using the automatic phonon library (APL) module in AFLOW. This method constructs a supercell of the original structure, displacing one or more atoms a distance of 0.015 Å from its equilibrium position. The forces generated by this displacement are used to determine the harmonic interatomic force constants (IFC), and these determine the phonon spectra in the harmonic approximation. Obviously the supercell must be large enough to minimize the interaction between images of the displaced atom, and the k-point mesh dense enough to map the intricacies of the supercell's electronic structure. We will discuss this in detail in Sec. VII.

(i) For α-Sn we used the standard face-centered cubic lattice vectors. APL calculations used a $4 \times 4 \times 4$ (128 atom) supercell and a $3 \times 3 \times 3$ Γ-centered k-point mesh, yielding 10 k points in the irreducible part of the supercell's Brillouin zone.

(ii) β-Sn has a very small value for c/a ($\approx$0.54), which required some special handling. We did our calculations using

the conventional tetragonal unit cell:

$$\begin{aligned}\vec{a}_1 &= a\,\hat{x}\\ \vec{a}_2 &= a\,\hat{y},\ \text{and}\\ \vec{a}_3 &= c\,\hat{z},\end{aligned} \tag{2}$$

which contains two primitive body-centered cubic cells and four tin atoms. APL calculations used a $3 \times 3 \times 5$ (180 atom) supercell, corresponding to a nearly-cubic $3a \times 3a \times 5c$ tetragonal cell. A $3 \times 3 \times 3$ Γ-centered k-point mesh was chosen, yielding 10 k points in the irreducible part of the supercell's Brillouin zone.

(iii) γ-Sn calculations used a $5 \times 5 \times 5$ (125 atom) supercell of the simple hexagonal lattice. The phonon spectra for this structure near Γ and the zone boundary was extremely sensitive to the choice of k-point mesh, and we finally settled on a $3 \times 3 \times 3$ Γ-centered mesh with 10 k points in the irreducible part of the supercell's Brillouin zone.

For a given unit cell volume V, we used VASP to find the value of c/a which minimized the total static lattice energy $U(V)$. We then used the AFLOW APL module to determine IFCs, the corresponding phonon spectrum and the phonon density of states, $g(V, \varepsilon)$ (pDOS).

With $g(V, \varepsilon)$ in hand we can determine all of the thermodynamic properties of the system. In particular, the energy due to the zero-point and thermal vibrations of the phonons is given by

$$U_{ph}(V, T) = \int_0^{\varepsilon_{\max}} g(V, \varepsilon) \left[\frac{\varepsilon}{2} + \frac{\varepsilon}{e^{\beta\varepsilon} - 1} \right] d\varepsilon, \tag{3}$$

where $\varepsilon_{\max}$ is the maximum phonon energy in the system. The first term in (3) is, of course, the zero-point energy, while the remainder is the thermal energy.

Since we are considering systems at volume V and temperature T, we must determine the Helmholtz free energy of the phonons,

$$F_{\text{ph}}(V, T) = U_{\text{ph}}(V, T) - T S_{\text{ph}}(V, T). \tag{4}$$

It is convenient to write this in the form [68]

$$\begin{aligned}F_{\text{ph}}(V, T) = \frac{1}{2} \int_0^{\varepsilon_{\max}} d\varepsilon\, g(V, \varepsilon)\, \varepsilon \\ + kT \int_0^{\varepsilon_{\max}} d\varepsilon\, g(V, \varepsilon)\, \ln(1 - e^{-\beta\varepsilon}).\end{aligned} \tag{5}$$

Again the first term in (5) is the zero-point energy of the phonons, while the remainder contains the temperature dependent contributions due to the phonons' vibrational energy and entropy. The second term is intrinsically negative and its magnitude increases with temperature, so $F_{\text{ph}}(V, T)$ is continually decreasing with temperature. It is weighted so that the lower frequency phonons make the largest contribution to the density of states, and this becomes more pronounced as the temperature increases. We can also see that the free energy is a weighted average over $g(V, \varepsilon)$ and so it will be insensitive to the exact behavior of the pDOS.

The free energy of the system as a function of volume and temperature is then

$$F(V, T) = U(V) + F_{\text{ph}}(V, T). \tag{6}$$

The temperature-dependent free energy of the system, $F(T)$, will be the minimum of (6) at temperature T. As we only find $F(V, T)$ at a few fixed volumes V_n, we approximate it by fitting the points $F(V_n, T)$ to a fourth-order Birch equation of state [69,70]:

$$F(V, T) = F(T) + \sum_{n=2}^{4} \gamma_n \left[\left(\frac{V_0(T)}{V} \right)^{2/3} - 1 \right]^n, \tag{7}$$

which gives us the system's free energy $F(T)$ and equilibrium volume $V_0(T)$ as a function of temperature.

We only need the primitive cell volume V to completely specify the structure of α-Sn. The β- and γ-Sn phases require that we also know the value of c/a, the ratio of the lattice constant in the z direction compared to the lattice constant in the x-y plane. A static lattice calculation will determine an energy $U(V, c/a)$. Fixing V and finding the minimum energy as a function of c/a will determine the energy $U(V)$ at that volume. As the value of c/a which minimizes (6) can change with temperature we should compute the corresponding free energy $F(V, c/a, T)$ and determine the free energy by minimizing (6) in both V and c/a at fixed T. This would be an enormous task. In practice the change in c/a with volume is so small during thermal expansion that this is not necessary, so we use the value of c/a determined by the static VASP calculation at all temperatures.

Visualizing and analyzing this data was accomplished using third-party software. In particular,

(i) The crystal structures shown in the Sec. II were plotted using Jmol [71].

(ii) Some of the experimental phonon frequencies appearing in the figures were taken from published graphs. We used the Engauge Digitizer [72] to convert this data into a form we could use. Any errors in the process are ours.

V. HIGH-THROUGHPUT CALCULATIONS AND CONVERGENCE

By their nature, high-throughput calculations rely on a set of standard assumptions, in particular that the basis set size (kinetic energy cutoff in a plane-wave code) and the density of the k-point mesh can be fixed without regard to the crystal structure being studied. For example, by default AFLOW sets the kinetic energy cutoff (ENMAX in VASP) to 140% of the minimum value recommended by VASP and the k-point mesh to give a minimum of 10000 k-points per reciprocal atom in the Brillouin zone [73], equivalent to a $22 \times 22 \times 22$ k-point mesh for a cubic system. While these standard values are usually sufficient, they may lead to errors when energy differences between phases are small.

We tested the reliability of the default energy cutoff and k-point size for tin by performing two sets of calculations to find the minimum energy configuration for the α-, β-, and γ-Sn phases described in Sec. II, looking at each of the functionals described in Sec. III. The first runs used the AFLOW default values of the energy cutoff and k-point mesh. The second set approximately doubled the energy cutoff and increased the k-point density in the Brillouin zone. The results are shown in Table II. There is little difference between the calculations' equilibrium values of V_0 and c/a with changing

TABLE II. Effect of changing the kinetic energy cutoff and k-point mesh density on the equilibrium properties of α-, β-, and γ-Sn, for the functionals shown. The left-hand column under each functional uses the AFLOW default kinetic energy cutoff (ENMAX) and k-point mesh (KMESH), while the right-hand column uses a higher energy cutoff and denser k-point mesh, as shown. Equilibrium volume (V_0) and c/a ratios are computed from the final configuration found by VASP. The volume V_0 is the volume of the primitive cell for each structure. The equilibrium energy difference $\Delta U(a, b)$ is defined as $U(a) - U(b)$ and given in meV/atom.

	LDA		PBE		PBEsol		AM05		revTPSS		SCAN	
ENMAX	144.6	350.0	144.6	350.0	144.6	350.0	144.6	350.0	144.6	350.0	144.6	350.0
						α-Sn						
KMESH	18×18×18	22×22×22	18×18×18	22×22×22	18×18×18	22×22×22	18×18×18	22×22×22	18×18×18	22×22×22	18×18×18	22×22×22
V_0 (Å^3)	67.976	67.957	73.601	73.589	69.587	69.587	70.094	70.106	70.093	70.121	69.969	69.947
						β-Sn						
KMESH	11×11×21	14×14×26	11×11×21	14×14×26	11×11×21	14×14×26	11×11×21	14×14×26	11×11×21	14×14×26	11×11×21	14×14×26
V_0 (Å^3)	52.387	52.415	56.714	56.708	53.453	53.489	53.335	53.382	53.089	53.167	54.630	54.585
c/a	0.540	0.540	0.540	0.541	0.540	0.540	0.540	0.541	0.540	0.540	0.536	0.538
						γ-Sn						
KMESH	22×22×21	28×28×26	22×22×21	28×28×26	22×22×21	28×28×26	22×22×21	28×28×26	22×22×21	28×28×26	22×22×21	28×28×26
V_0 (Å^3)	26.221	26.219	28.378	28.387	26.757	26.755	26.699	26.697	26.543	26.561	27.242	27.253
c/a	0.945	0.939	0.946	0.940	0.946	0.939	0.946	0.939	0.944	0.939	0.945	0.939
						Equilibrium energy differences (meV/atom)						
$\Delta U(\beta, \alpha)$	−22.739	−22.928	39.442	38.726	−28.896	−29.531	−4.878	−5.784	−85.814	−87.303	73.569	73.579
$\Delta U(\gamma, \alpha)$	−18.527	−19.758	40.033	38.188	−26.389	−28.239	−2.547	−5.018	−82.689	−86.410	79.448	79.881
$\Delta U(\gamma, \beta)$	4.212	3.170	0.591	−0.538	2.507	1.292	2.331	0.767	3.125	0.894	5.879	6.301

TABLE III. Predicted equilibrium properties of α-, β-, and γ-Sn for the density functionals described in Sec. III using the default AFLOW parameters for each structure from Table II. These calculations were made by allowing VASP to fully relax each unit cell. $\Delta U_{\alpha\beta}$ and $\Delta U_{\alpha\gamma}$ represent the equilibrium energy difference between β-Sn or γ-Sn and α-Sn, respectively. A positive number indicates that α-Sn is lower in energy. We also include experimentally measured lattice constants for comparison, using the alloy with stoichiometry $Sn_{0.8}In_{0.2}$ [14] as a stand-in for γ-Sn.

	α-Sn	β-Sn		γ-Sn		$\Delta U_{\alpha\beta}$	$\Delta U_{\alpha\gamma}$
	a (Å)	a (Å)	c (Å)	a (Å)	c (Å)	(eV/atom)	(eV/atom)
Expt. (90 K)	6.483 [74]						
Expt. (100 K)		5.815 [75]	3.164 [75]				
Expt. (296 K)	6.491 [19]	5.832 [75]	3.183 [75]	3.216 [14]	2.998 [14]		
Expt. (300 K)		5.8315 [76]	3.1828 [76]				
LDA	6.4785	5.7905	3.1248	3.1762	3.0012	−22.739	−18.527
PBE	6.6524	5.9455	3.2089	3.2593	3.0847	39.442	40.033
PBEsol	6.5292	5.8293	3.1461	3.1968	3.0233	−28.896	−26.389
AM05	6.5451	5.8227	3.1463	3.1947	3.0208	−4.878	−2.547
revTPSS	6.5450	5.8139	3.1412	3.1897	3.0124	−85.814	−82.689
SCAN	6.5412	5.8845	3.1553	3.2163	3.0409	73.569	79.448

basis set size/k-point mesh. There is a larger discrepancy in the energy differences. The "worst case" seems to be the revTPSS functional, where ΔU for the β-Sn phase shifts by 3.7 meV/atom when we change basis sets. SCAN is the "best" functional, as the largest shift in ΔU is only 0.43 meV/atom for β-Sn. Most shifts are on the order of 1–3 meV/atom, which will not be large enough to change our conclusions.

There are some interesting anomalies in the last three lines of Table II. As α-Sn is the ground state and γ-Sn is the highest temperature state, we would expect $U_{\gamma-\mathrm{Sn}} > U_{\beta-\mathrm{Sn}} > U_{\alpha-\mathrm{Sn}}$, where all of the ΔU values should be positive. SCAN is the only functional to achieve this in both the standard and higher precision calculations. PBE correctly states that the ground state energies of both β- and γ-Sn are well above that of α-Sn, but the sign of the energy difference between those two phases changes when we go from the lower accuracy calculation to the higher. All other functionals predict β-Sn to have the lowest energy of the three structures and α-Sn the largest.

While it is desirable to have highly converged results, the calculation of thermal properties in tin requires a large number of calculations, so we would like to keep the energy cutoff and k-point mesh as small as possible to speed up the calculations. For this reason we will use the low energy cutoff (144.6 meV) and smaller k-point mesh for all of our calculations. The only place this might cause difficulties is when we use the PBE functional, which switches the ordering of β- and γ-Sn when we switch basis set size. As we shall see below, the change in the vibrational free energy (5) between these phases will be much larger than the change in static energy.

VI. ELECTRONIC STRUCTURE AND ENERGY

The first quantity needed to compute the free energy (6) is the energy $U(V)$ of the static lattice. Here we discuss the results of the calculations for $U(V)$ for all of the density functionals in Sec. III, using the default of ENMAX and KMESH listed in Table II. The minimization in energy versus c/a at fixed volume is controlled by VASP. We also look at the electronic structure for α-, β-, and γ-Sn at the equilibrium structures shown in Table III, confirming that α-Sn is a semimetal and the other two structures are metals. All of the calculations use the smaller energy cutoff and k-point mesh listed in Table II.

A. The local density approximation (LDA)

Figure 2 shows the electronic density of states (eDOS) for tin in α-, β-, and γ-Sn at equilibrium (Table III) within the local density approximation (LDA). As we expect, α-Sn is a semimetal. Both β- and γ-Sn are metals with approximately the same density of states near the Fermi level, an unsurprising result given the close connection of the two structures discussed in Sec. II.

The predicted energy-volume curves are shown in Fig. 3. As is usual with the LDA the predicted equilibrium volume for β-Sn is about 4% below the experimental volume. Somewhat surprisingly the equilibrium volume for α-Sn is approximately equal to the low-temperature experimental volume.

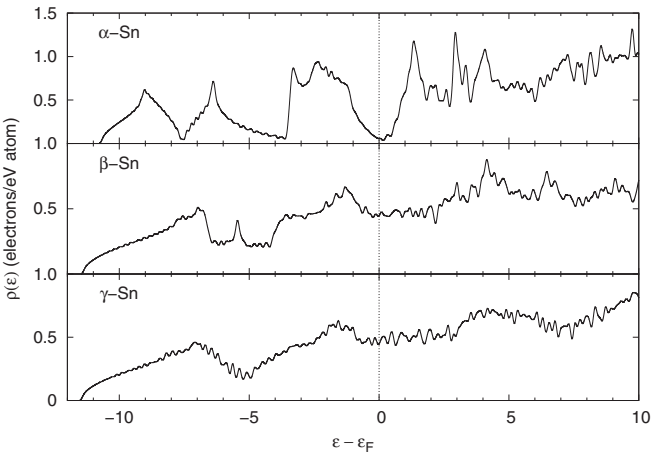

FIG. 2. Electronic density of states for α-, β-, and γ-Sn computed using the LDA at the equilibrium structure of each phase found in Table III.

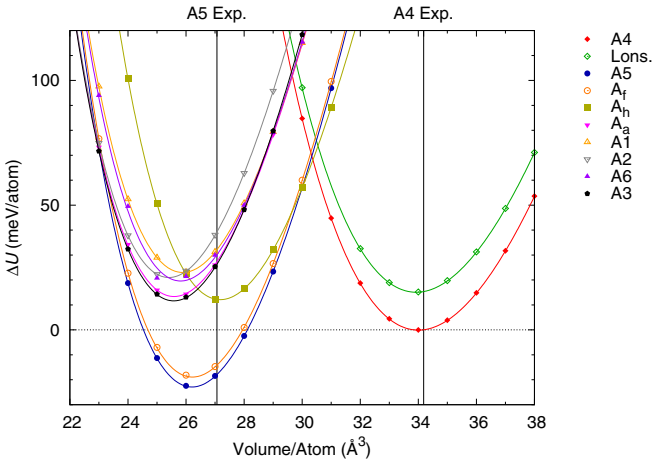

FIG. 3. Static lattice energy-volume curves for the tin structures discussed in Sec. II as predicted by AFLOW/VASP using the LDA functional. Structural notation is from Table I. We plot ΔU, the change in energy per atom compared to the equilibrium energy of the α-Sn ($A4$) structure. The lines labeled "A5 Expt." and "A4 Expt." represent the experimental volume of β-Sn ($A5$) at 298 K [77] and α-Sn ($A4$) at 90 K [74], respectively.

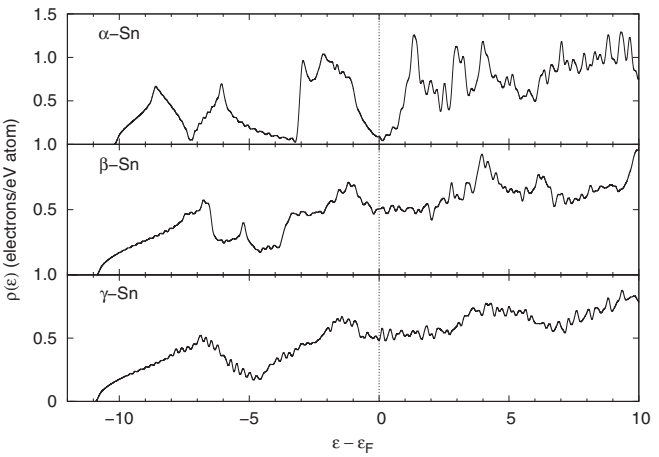

FIG. 4. Electronic density of states for α-, β-, and γ-Sn computed using the PBE functional at the equilibrium structure of each phase found in Table III.

As one expects there is a large equilibrium volume difference between α- and β-Sn, in agreement with experiment. In addition, Lonsdaleite ("Lons." in the figure), the hexagonal diamond structure, is correctly above α-Sn ($A4$), and γ-Sn (A_f) is above β-Sn ($A5$). We see that the LDA overbinds both β-Sn and γ-Sn with respect to α-Sn, contrary to experiment, predicting a β-Sn ground state. In addition, γ-Sn is nearly degenerate with β-Sn, in agreement with the calculations of Wehinger *et al.* [47].

Christensen and Methfessel [78] also found β-Sn as the ground state within the LDA using the LMTO-ASA method. Their equilibrium energy difference was 5 meV/atom, substantially less than our value of 20 meV/atom, but neither result will support the experimentally observed structural transition.

B. The Perdew-Burke-Ernzerhof generalized gradient functional (PBE)

Figure 4 shows the electronic density of states at equilibrium for the three phases of interest. The results are very similar to the LDA.

The PBE results for $U(V)$ are shown in Fig. 5. As is usual with the PBE the predicted equilibrium volumes are 3–10% above the experimental values. The PBE is an improvement over LDA as it finds that the equilibrium energy of the β-Sn phase is almost 40 meV above the α-Sn, in agreement with previous work [21]. As with LDA, the β- and γ-Sn phases are nearly degenerate. Using the small energy cutoff and k-point mesh found in Table II we find β-Sn below γ-Sn, but this will reverse if we increase the basis set size. As we will see below thermal effects will dwarf this energy difference.

C. The Perdew-Burke-Ernzerhof generalized gradient functional revised for solids (PBEsol)

The electronic density of states and energy volume curves for the PBEsol functional are shown in Figs. 6 and 7. Since this functional was designed to give better equilibrium volumes than PBE, it is not surprising that the equilibrium volumes for the α, β, and γ phases are between those predicted by the LDA and PBE functionals. The eDOS curves are very similar to those of the LDA.

In other respects the PBEsol results are slightly worse than those found by the LDA. The β-Sn phase is even more bound compared to the α phase, and the β and γ phases are closer together, though not as close as found with the PBE.

D. The Armiento-Mattsson generalized gradient functional (AM05)

The results for the AM05 functional are shown in Figs. 8 and 9. Again the eDOS is similar to the LDA and nearly

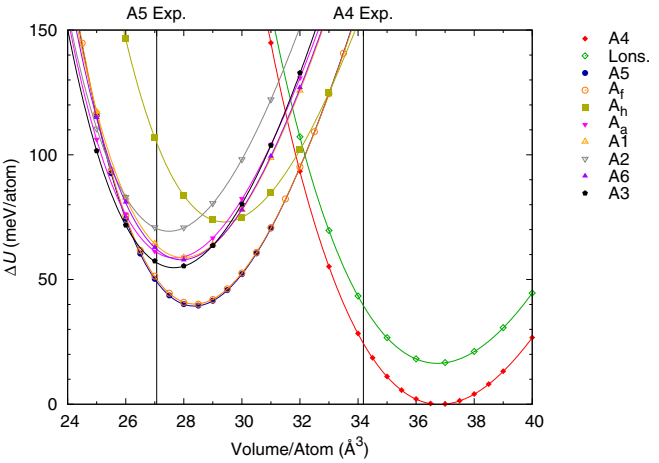

FIG. 5. Static lattice energy-volume curves for the tin structures discussed in Sec. II as predicted by AFLOW/VASP using the PBE functional. The notation is identical to that in Fig. 3.

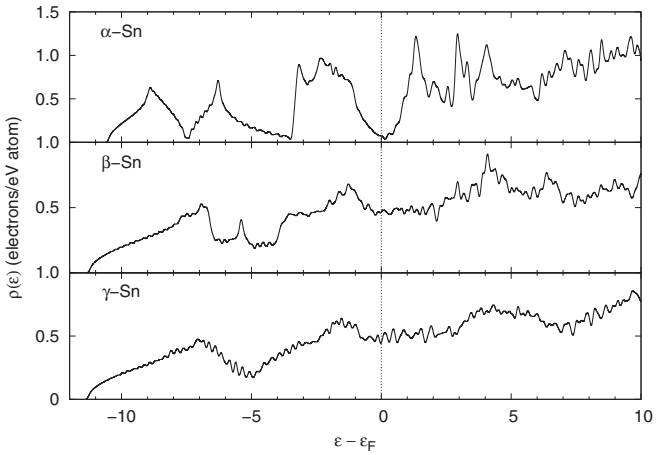

FIG. 6. Electronic density of states for α-, β-, and γ-Sn computed using the PBEsol functional at the equilibrium structure of each phase found in Table III.

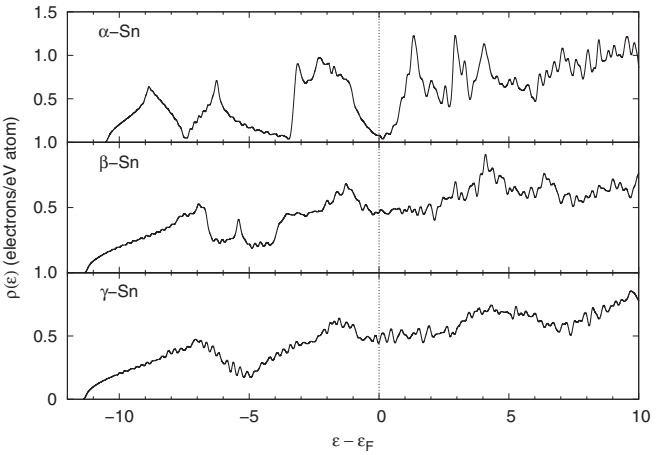

FIG. 8. Electronic density of states for α-, β-, and γ-Sn computed using the AM05 functional at the equilibrium structure of each phase found in Table III.

identical to the PBEsol result. The equilibrium properties are also similar to PBEsol, except that the β- and γ-Sn phases are closer to diamond than they are in LDA or PBEsol calculations.

It is interesting to look at the close-packed ($A1$, $A3$) and near close-packed ($A2$, $A6$, A_a) phases in this study. The previous functionals predicted that these phases had minimum energies 20–40 meV/atom above β- and γ-Sn. Here the energy difference is only about 5 meV/atom. Even ignoring the misplaced α-Sn phase, this small energy difference leads to a prediction of a transition from β-Sn to body-centered cubic Sn at 1 GPa, far below the observed experimental transition at 35 GPa [79].

E. Meta-GGA functionals (except SCAN)

With the exception of the SCAN functional discussed below, all of the meta-GGA functionals (TPSS, revTPSS, MS0/1/2, M06-L), significantly overbind the close-packed fcc ($A1$) and hcp ($A3$) structures, as well as the nearly close-packed bcc ($A2$) structure and the tetragonal $A6$ and A_a structures. Calculations using these functionals are significantly more time consuming than LDA or GGA calculations, so once we realized this, we screened the functionals by looking at the energy difference between the hcp ($A3$) and α-Sn ($A4$) phases. To show the trend in these systems we did a complete set of energy/volume calculations using the revTPSS functional and show these results in Figs. 10 and 11. The electronic density of states for the tin phases are similar to those obtained by other functionals, but all of the close-packed and nearly close packed phases are well below the experimentally observed tin phases. In addition, β- and γ-Sn are overbound by 70 meV/atom compared to the experimental ground state, α-Sn. These functionals have been optimized for noncovalent interactions [61] so it is not surprising that they do not describe the energetics of the covalently-bonded α-Sn phase particularly well.

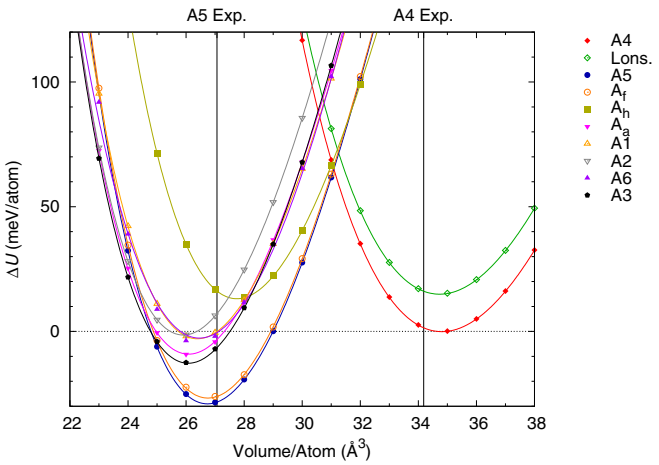

FIG. 7. Static lattice energy-volume curves for the tin structures discussed in Sec. II as predicted by AFLOW/VASP using the PBEsol functional. The notation is identical to that in Fig. 3.

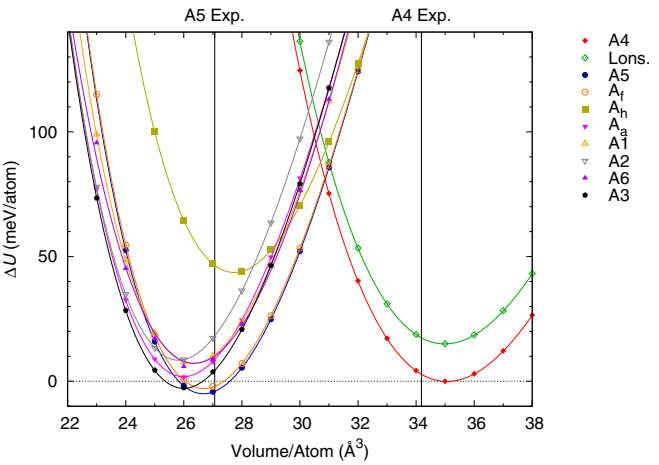

FIG. 9. Static lattice energy-volume curves for the tin structures discussed in Sec. II as predicted by AFLOW/VASP using the AM05 functional. The notation is identical to that in Fig. 3.

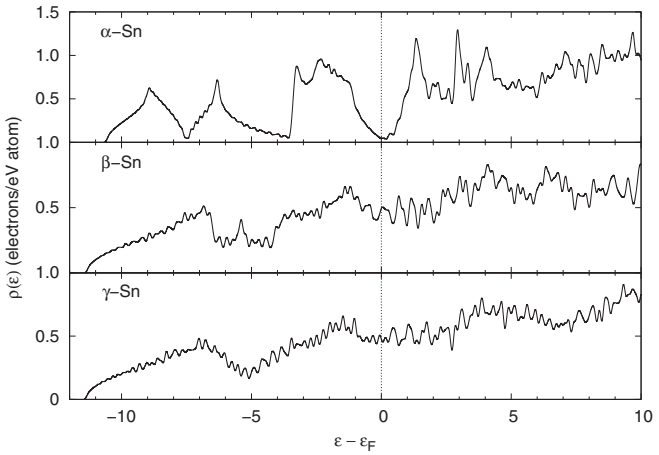

FIG. 10. Electronic density of states for α-, β-, and γ-Sn computed using the revTPSS functional at the equilibrium volume for each structure found in Table III.

F. The strongly constrained and appropriately normed (SCAN) meta-GGA

Unlike meta-GGAs such as M06-L, the SCAN functional is nonempirical and is designed "to satisfy all 17 exact constraints appropriate to a semilocal functional" [63]. The SCAN electronic density of states, Fig. 12, correctly finds the semimetallic behavior of α-Sn and the metallic behavior of β- and γ-Sn. As shown in Fig. 13, SCAN predicts the correct ordering of the major tin phases, $U_{\alpha-\mathrm{Sn}} < U_{\beta-\mathrm{Sn}} < U_{\gamma-\mathrm{Sn}}$. The simple cubic ($A_h$) phase is very low compared to other calculations, while the close-packed and nearly close-packed phases barely make the graph, with only the body-centered tetragonal α-Pr (A_a) phase within 200 meV of α-Sn.

G. Summary of DFT calculations for the ground state of tin

Table III provides a brief summary of the equilibrium properties of the three tin phase for each choice of DFT, along with the static energy difference between the three phases.

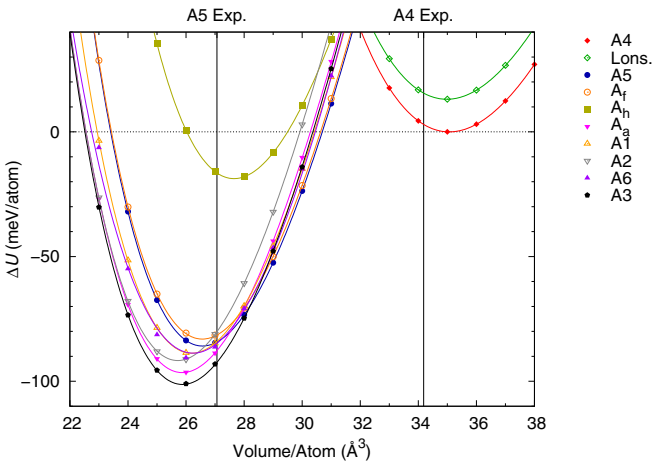

FIG. 11. Static lattice energy-volume curves for most of the tin structures discussed in Sec. II as predicted by AFLOW/VASP using the revTPSS functional. The notation is identical to that in Fig. 3.

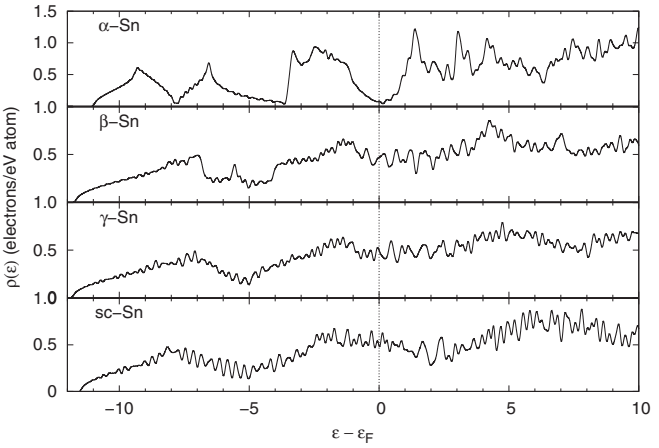

FIG. 12. Electronic density of states for α-, β-, γ-Sn computed using the SCAN functional at the equilibrium volume for each structure found in Table III. We also include the DOS of simple cubic tin at its SCAN equilibrium structure, $a = 3.0432$ Å.

The SCAN functional is the only one which correctly predicts the energy relationship $U(\alpha\text{-Sn}) < U(\beta\text{-Sn}) < U(\gamma\text{-Sn})$ for all choices of basis set and k-point mesh. In that sense it is better than any of the other functionals studied. Unfortunately the relative energy $U(\beta\text{-Sn}) - U(\alpha\text{-Sn})$ is approximately 80 meV/atom, significantly larger than the 10–40 meV/atom suggested by the 286 K transition temperature [17,18], and like most of the functionals discussed here it overestimates the equilibrium volumes for both white and gray tin.

VII. PHONON CONVERGENCE AND ACCURACY

When we determine the vibrational free energy F_{ph} (5) of the various phases of tin, we must consider both convergence and accuracy. We will say that the calculations are converged if the $F_{\mathrm{ph}}(T)$ is insensitive to the size of the supercell and k-point mesh. By accuracy we mean that our computed phonon

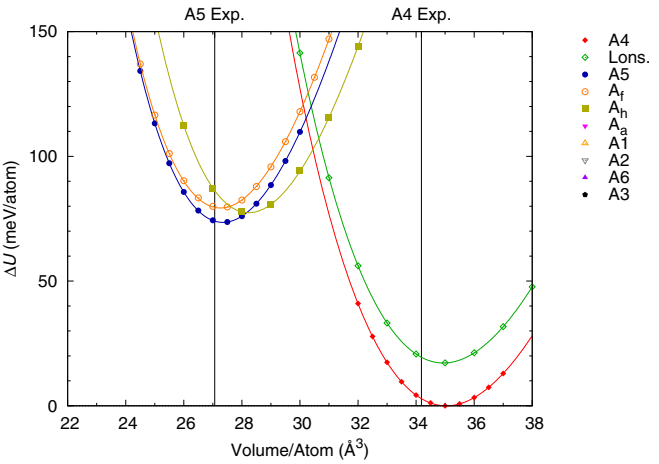

FIG. 13. Static lattice energy-volume curves for the tin structures discussed in Sec. II as predicted by AFLOW/VASP using the SCAN functional. The notation is identical to that in Fig. 3. Structures not shown ($A1, A2, A3, A6$) are above the $\Delta U = 150$ meV/atom limit of the graph.

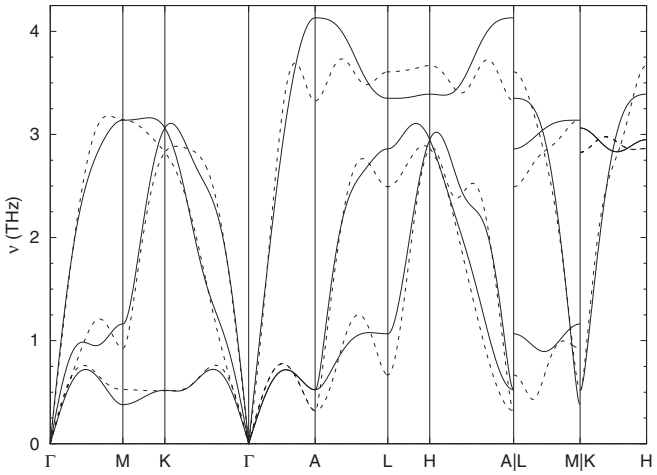

FIG. 14. Phonon spectra of γ-Sn using the PBE functional at equilibrium as given in Table II. The solid line shows the results for the 125 atom supercell, while the dashed line shows the 216 atom supercell. The high-symmetry paths through the face-centered cubic Brillouin zone are defined by Setyawan and Curtarolo [80].

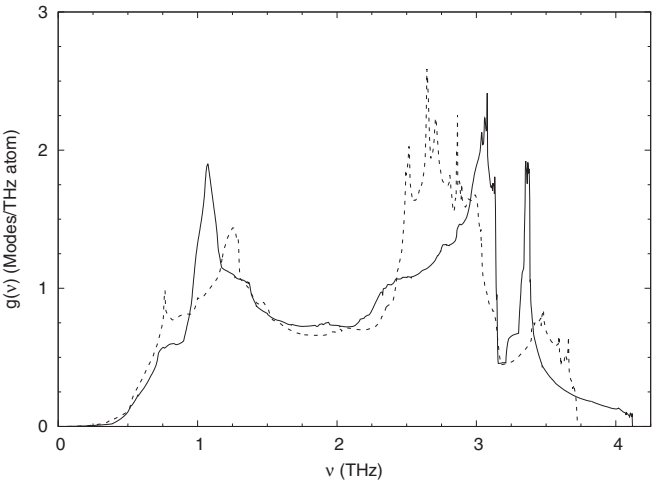

FIG. 15. Phonon density of states for the same cell described in Fig. 14. The solid line shows the results for the 125 atom supercell, while the dashed line shows the 216 atom supercell. The density of phonon modes is normalized for one atom, so the area under each curve is equal to three.

frequencies agree with experiment. Obviously we can never be perfectly converged nor perfectly accurate, but this perfection is not needed to obtain a reasonable value of $F_{\rm ph}$. The zero-point and thermal free energy integrals in (5) perform a weighted average of the phonon density of states $g(V, \varepsilon)$. The thermal contribution to the free energy is weighted toward the low frequency end of the phonon spectrum, where the Debye modes dominate. Small differences between the phonon density of states calculated from two different supercells, or between the computed and experimental pDOS, will be minimized by the averaging process.

To see this, consider a calculation of the phonon frequencies of γ-Sn. We will look at the phonons predicted by the PBE functional, using the equilibrium structure described in Table II. (In all of the following we will use the default AFLOW energy cutoff, 144.6 meV.) In the first case we consider a $5 \times 5 \times 5$ supercell with 125 atoms, and the second a $6 \times 6 \times 6$ cell with 216 atoms. In both cases we use a $3 \times 3 \times 3$ Γ-centered k-point mesh, yielding 10 k points in the Brillouin zone.

Figure 14 shows the phonon spectrum for both cells. There are considerable differences, especially at the "A" point $(00\frac{1}{2})$, where the smaller cell finds the highest frequency almost 0.5 THz greater than found for the larger cell. Figure 15 shows the phonon density of states for the two calculations. Now we see general agreement between the two calculations. Except for a disagreement in the pDOS near 1 THz, the two curves are in agreement up to nearly 2.5 THz. In Fig. 16 even these differences are washed out as we compute the vibrational free energy. The difference in the free energy of the two calculations only reaches 3 meV, a 0.5% difference, at 1000 K. The zero point energy for the 126 atom cell is 13.67 meV, while it is 13.50 meV for the 216 atom cell, a difference of 1.3%.

We get even better results for α-Sn. Figure 17 shows the vibrational free energy of α-Sn at equilibrium using the PBE functional using $4 \times 4 \times 4$ (128 atom) and $5 \times 5 \times 5$ (250 atom) supercells. The agreement here is even better, with less than 0.2% difference in the free energy at 1000 K. The zero point energy is 10.539 meV/atom for the smaller cell and 10.544 meV for the larger, a 0.04% discrepancy.

Finally, the PBE vibrational free energy of β-Sn is shown in Fig. 18, where we compare a $3 \times 3 \times 5$ (180 atom) supercell to a $4 \times 4 \times 7$ (448 atom) cell. The difference between the two calculations at 1000 K is 0.5%. At 0 K the zero point energy is 14.33 meV for the small cell and 14.20 meV for the large cell, a 0.9% discrepancy, on the same order as the error in γ-Sn.

We have also investigated k-point convergence in the supercells by increasing the k-point mesh in all three supercells. $F_{\rm ph}$ for α-Sn and β-Sn are well converged with k-point mesh using the default APL values (Γ-centered $3 \times 3 \times 3$ meshes

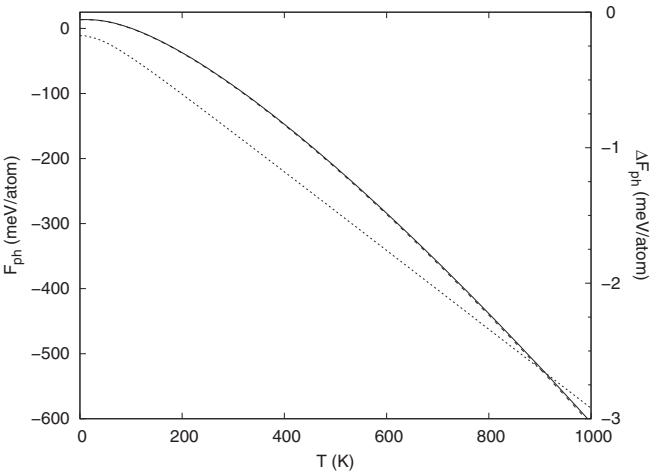

FIG. 16. Vibrational free energy (5) for the same cell described in Fig. 14. The left axis shows $F_{\rm ph}$ for the 126 atom supercell (solid line) and the 216 cell (dashed line). The dotted line is the difference in the vibrational free energy between the cells, with the scale on the right.

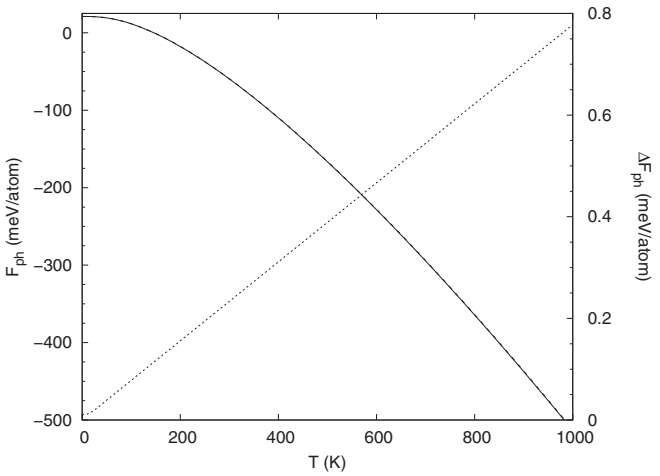

FIG. 17. Vibrational free energy (5) for α-Sn using the PBE functional at equilibrium (Table II). The left axis shows F_{ph} for the 128 atom supercell (solid line) and the 250 atom supercell (the barely distinguishable dashed line). The dotted line is the difference between the cells, with the scale on the right.

with 10 k points in the irreducible Brillouin zone for both systems). γ-Sn gives imaginary phonons for meshes which are not of the form $3n \times 3n \times m$, where m and n are integers. This is presumably because the behavior of the hexagonal system strongly depends on the electronic structure near the Brillouin zone boundary. The $6 \times 6 \times 4$ k-point mesh gives values for F_{ph} close to that of the $3 \times 3 \times 3$ mesh, so this phase is converged as well.

We conclude that the supercells we have chosen are adequate to determine the vibrational free energy below 1000 K with an accuracy of $\approx$1.4% or better. But do our phonon calculations actually correspond to reality? Since we have experimental phonon results for all three phases of tin or a tin alloy we can compare these to our results.

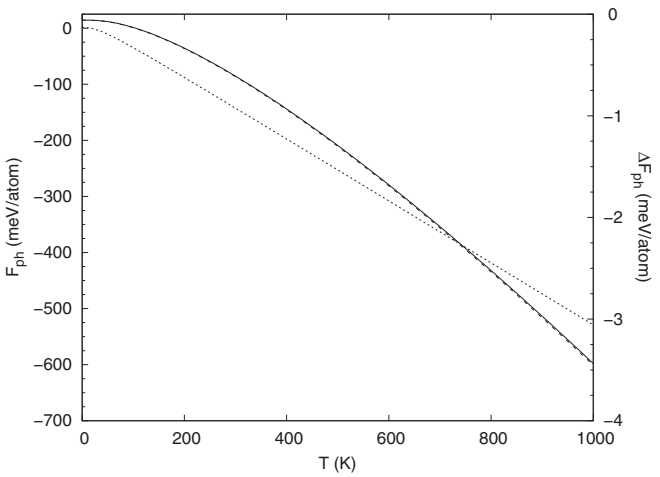

FIG. 18. Vibrational free energy (5) for β-Sn using the PBE functional at equilibrium (Table II). The left axis shows F_{ph} for the 180 atom supercell (solid line) and the 448 atom supercell. The dotted line is the difference between the cells, with the scale on the right.

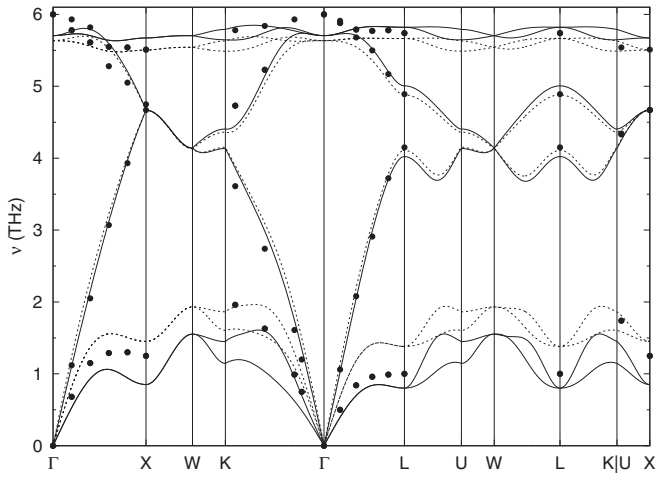

FIG. 19. Phonon spectra of α-Sn at the experimental volume. The solid lines are the frequencies predicted using the APL module of AFLOW with the PBE functional, and the dashed lines are the predicted frequencies for the SCAN functional. The circles are the frequencies measured by Price *et al.* [74] at 90 K. The calculations use the supercell described in Sec. IV. The high-symmetry paths through the face-centered cubic Brillouin zone are defined by Setyawan and Curtarolo [80]. Note that Price *et al.* only determined the frequencies of one of the transverse branches along the Γ-K and U-X directions (the Σ line).

Phonon data for α-Sn (gray tin, *Strukturbericht* $A4$) was obtained by Price *et al.* [74] at 90 K, with a unit cell volume of 68.1 Å^3. We compare our results with theirs along high-symmetry lines in the Brillouin zone [80] in Fig. 19. The calculations are reasonably good, better for the optical modes and longitudinal acoustic modes than for the transverse acoustic modes. We will see below that the optical modes in α-Sn dominate the free energy, so this is acceptable. Aouissi *et al.* [81] have shown that it is possible to get extremely accurate computational phonon spectra for α-Sn, but this requires supercells larger than we can afford to use and get this work finished in a reasonable time.

Rowe *et al.* [75] and Price [76] measured the phonon spectrum of β-Sn (white tin, *Strukturbericht* $A5$) at 296 K and 300 K respectively, finding a volume of 54.1 Å^3. The results are shown in Fig. 20. The agreement with experiment is worse than it was for α-Sn in the optic modes, but better in the acoustic modes. Since the acoustic modes dominate the free energy in β-Sn, this, too, is acceptable.

There are no samples of simple hexagonal (*Strukturbericht* A_f) tin, but alloying with indium is known to stabilize this phase. Ivanov *et al.* [14] measured the phonon spectrum of γ-Sn $Sn_{0.8}In_{0.2}$ at room temperature, where they found the sample to have a primitive cell volume of 26.8 Å^3. We compare that to our calculations for pure simple hexagonal tin in Fig. 21. Here the agreement for longitudinal mode and the upper transverse mode is excellent. There is some error in the lower transverse mode, on the order of that in α-Sn.

While the APL is generally reliable, as shown above, there are points where it gives imaginary phonon frequencies. In particular, SCAN predicts that γ-Sn has an unstable phonon mode at M ($\frac{1}{2}$00) for cell volumes $\geqslant$30 Å^3. It may be that this

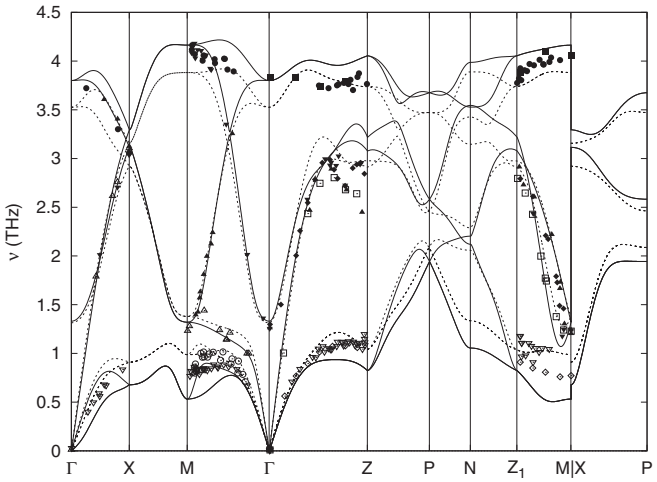

FIG. 20. Phonon spectra of β-Sn at the experimental volume. The solid lines are the frequencies predicted using the APL module of AFLOW with the PBE functional, and the dashed lines are the predicted frequencies for the SCAN functional. In both cases the volume is held fixed, but the value of c/a is chosen to minimize the total energy. The calculations use the supercell described in Sec. IV. The circles are the frequencies measured by Price [76] at 300 K and Rowe *et al.* [75] at 296 K. The high-symmetry paths through the body-centered tetragonal Brillouin zone are defined by Setyawan and Curtarolo [80]. Note that Price only determined the frequencies of one acoustic and one optic transverse branch along the Γ-X (Δ) line. Data points were obtained from the references using the Engauge Digitizer [72].

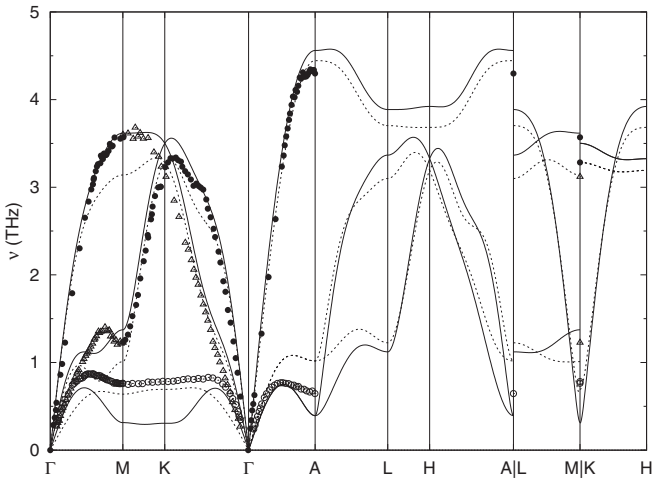

FIG. 21. Phonon spectra of computational γ-Sn and experimental $Sn_{0.8}In_{0.2}$ at the experimental volume. The solid lines are the frequencies predicted using the APL module of AFLOW with the PBE functional, and the dashed lines are the predicted frequencies for the SCAN functional. In both cases the volume is held fixed, but the value of c/a is chosen to minimize the total energy. The calculations use the supercell described in Sec. IV. The circles are data taken by Ivanov *et al.* [14] for $Sn_{0.8}In_{0.2}$ at room temperature. The high-symmetry paths through the simple hexagonal Brillouin zone are defined by Setyawan and Curtarolo [80]. Data points were obtained from the references using the Engauge Digitizer [72].

is an indication that the γ-Sn structure is unstable with respect to β-Sn, but we have not investigated this point. Fortunately the thermal expansion of tin does not take us past this critical volume so long as we keep the temperature below 800 K, which is sufficient for this study.

Finally, we should stress that all of these calculations are carried out in a quasiharmonic approximation, assuming that the vibrational energy of each phonon mode is quadratic in the displacement of the atoms and that the IFCs only depend on the structure and the volume of the unit cell. Since tin melts at 505 K [82] we are obviously close to the failure of the quasiharmonic approximation, but the consideration of nonquadratic behavior is beyond the scope of this work.

VIII. PHONONS AND THERMODYNAMICS

The free energy $F(T)$ has two major contributions: the static lattice energy $U(V)$ determined by VASP, and the vibrational free energy $F_{\rm ph}(T)$ (5), found from the phonon density of states $g(V,\varepsilon)$. The behavior of the second term obviously dominates the thermal behavior of tin. If we look at the graphs of $U(V)$ in Section VI we see that a volume change of 10% changes the energy by 10–20 meV/atom. The vibrational free energy discussed in Sec. VII changes by hundreds of meV/atom going from absolute zero to 500 K.

The AFLOW APL module allows us to determine $g(V,\varepsilon)$ and find the zero-point and temperature-dependent free energy for all three of the tin phases. The procedure is as follows:

(i) Determine the equilibrium c/a and static energy $U(V)$ of the three possible phases of tin as a function of volume using AFLOW/VASP. Since the variation of c/a for the β and γ phases is small, we will ignore changes in c/a with temperature and use the c/a found to minimize the static energy at each volume for all temperatures at that volume.

(ii) Use AFLOW's APL module to determine the phonon spectra for each structure and volume.

(iii) The APL module finds the pDOS and then determines the vibrational free energy (6) as a function of temperature for each of these structures and volumes, including the zero-point energy.

(iv) For a given temperature, determine the volume which minimizes the free energy using the Birch fit (7), generating the free energy $F(T)$ and equilibrium volume $V(T)$.

(v) Determine the averaged linear expansion coefficient of each structure using the relationship

$$\alpha(T) = \frac{1}{3V(T)}\frac{dV}{dT}(T), \tag{8}$$

where $V(T)$ is the unit cell volume of the crystal. For the tetragonal β and hexagonal γ phases $\alpha(T)$ will be the average of the linear expansion coefficients in the x, y, and z directions. By default the APL module prints $F(V,T)$ in 10 K increments from absolute zero to 2000 K. We determine the equilibrium $V(T)$ from (7) and use five-point numerical differentiation of these results to find $\alpha(T)$.

(vi) Compare the values of the free energy $F(T)$ for each structure to determine the equilibrium structure as a function of temperature.

TABLE IV. Zero-point energy (9) for a variety of density functionals. All calculations are performed at the equilibrium lattice constants given in Table III and use the k-point meshes described in Sec. VII. The structures marked with an asterisk have imaginary modes. The ZPE for these structures were calculated by only integrating over the real modes.

Functional	α-Sn	β-Sn	γ-Sn
LDA	22.4	16.3	15.5
PBE	21.1	14.4	13.7
PBEsol	21.8	15.9	15.1
AM05	21.8	16.0	15.0
revTPSS	21.7	16.2*	15.3*
SCAN	22.5	15.5	14.4

A. Zero-point energy

The PBE and SCAN functionals correctly place the static equilibrium energies of β- and γ-Sn above α-Sn. Neither the LDA, PBEsol, nor AM05 functionals correctly order these phases, all making β-Sn the ground state. The revTPSS and other non-SCAN metaGGA functionals predict a close-packed phase to be the ground state but also predict the β-Sn phase to be lower in energy than the other two tin phases. The obvious conclusion is that we should only concentrate on the PBE and SCAN calculations, but we must remember that the vibrational free energy, in particular the zero-point energy, is not directly related to the static energy $U(V)$.

In that case, since the energy differences between the phases are rather small, especially for AM05, the zero-point energy (ZPE) in (5) might change the ordering of the phases. The ZPE might even change the α-β energy difference found in the SCAN functional to make it closer to that found using PBE.

While the ZPE is implicitly contained in the calculations in the next two parts of this section, there we will only discuss "interesting" functionals. Here we will discuss the ZPE for all the functionals we studied.

As we showed in Sec. IV, the ZPE is just half of the average phonon energy as weighted by the pDOS:

$$F_{\mathrm{ZPE}}(V) = \frac{1}{2}\int_0^{\varepsilon_{\max}} d\varepsilon\, g(V,\varepsilon)\,\varepsilon. \tag{9}$$

We used the APL module to compute the zero-point energy at static equilibrium, as given in Table III, for a variety of density functionals, presenting our results in Table IV. The revTPSS calculations show that β- and γ-Sn are unstable, with imaginary frequencies near Γ (β-Sn) and M (γ-Sn), not surprising as these structures are not the lowest ones at their equilibrium volumes. The ZPE for these states only includes the real modes and is presented only for comparison.

In all other cases we find that the zero-point energy of α-Sn is 35–45% larger than that of the β- or γ-Sn phases. This can be easily explained by looking at the phonon density of states for the three phases. Figure 22 shows the pDOS for all three phases using both the PBE and SCAN functionals. Other functionals give similar results. We see that the covalent bonding in α-Sn produces a phonon spectrum almost perfectly

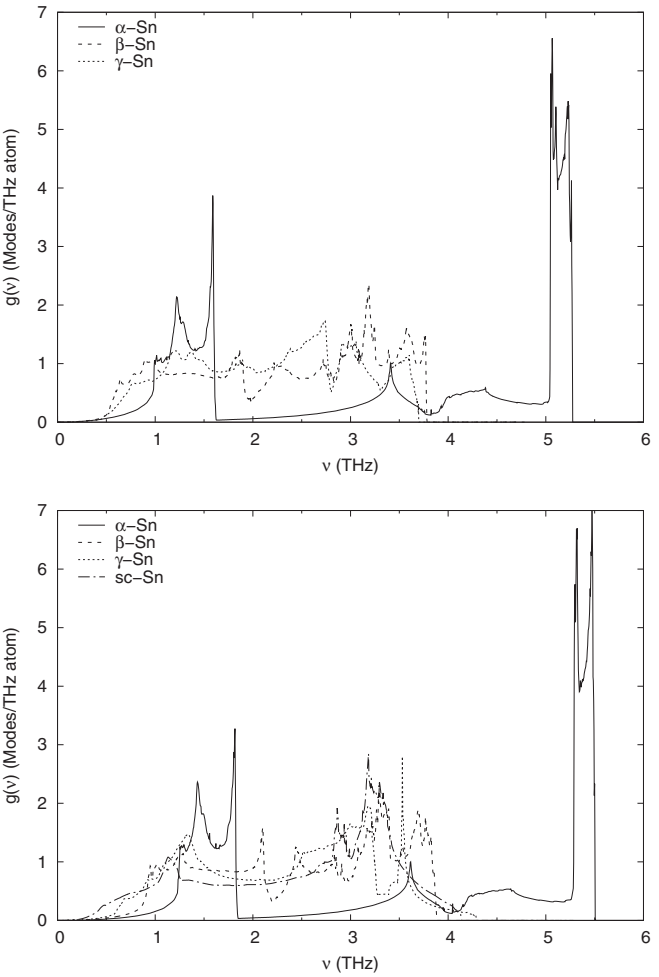

FIG. 22. Phonon density of states for α- (solid line), β- (dashed line) and γ-Sn (dotted line) at the equilibrium configurations from Table III. Top panel: PBE functional. Bottom panel: SCAN functional. We show the number of phonon modes per atom, thus the area under each curve is three.

divided into acoustic and optical modes. The optical modes are concentrated near the top of the phonon conduction band, and the maximum phonon frequency for α-Sn is roughly 20% larger than the maximum of the other two phases. As a result the zero-point energy (9) of α-Sn will always be larger than that of the other two phases. This means that if the static lattice calculation predicts that the β- or γ-Sn phase is the ground state, then the addition of zero-point energy will increase the energy difference. Consequently the LDA, PBEsol, AM05, and revTPSS functionals will never find the experimentally observed ordering between phases. The zero-point energy *will* decrease the observed energy difference between α-Sn and the other structures when using the PBE and SCAN functionals, and so will lower the α-β-γ phase transitions temperature compared to what would be found with no zero-point energy.

Table IV also shows that the zero-point energy of γ-Sn is *always* lower than the zero-point energy of β-Sn. This will be important when we discuss the thermal stability of tin below.

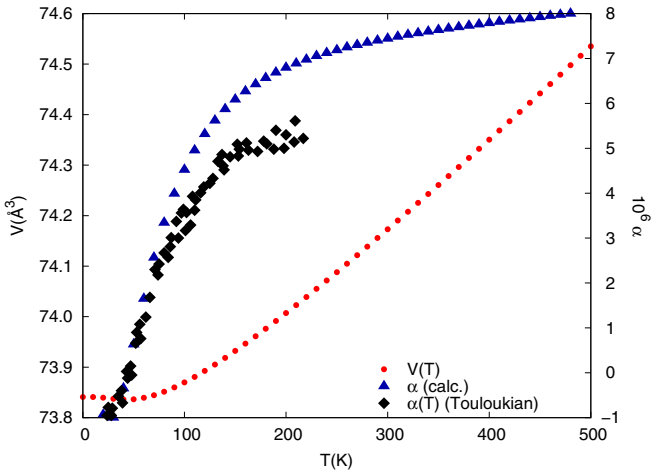

FIG. 23. The primitive-cell volume of α-Sn as a function of temperature (left axis, red circles) and the linear expansion coefficient α (right axis, blue triangles) calculated by APL using the PBE density functional. We also plot the experimental data found in Touloukian *et al.* [83] (black diamonds).

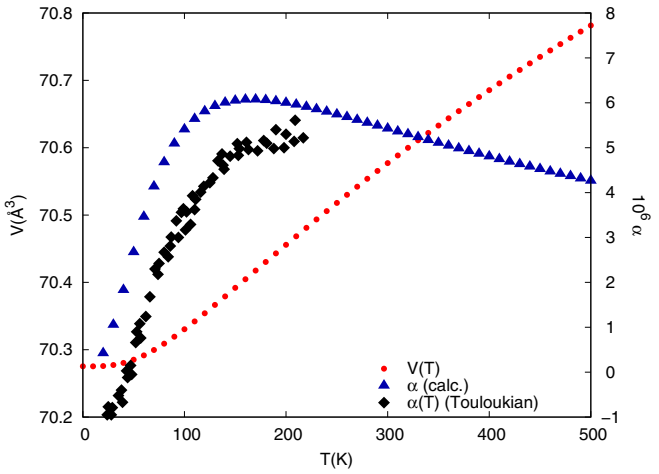

FIG. 24. The primitive-cell volume of α-Sn as a function of temperature (left axis, red circles) and the linear expansion coefficient α (right axis, blue triangles) calculated by APL using the SCAN density functional. We also plot the experimental data found in Touloukian *et al.* [83] (black diamonds).

B. Thermal expansion

We now look at the full effect of the phonons on the thermodynamics of tin predicted by these functionals. First we consider the thermal expansion of the tin structures. The APL module of AFLOW prints the vibrational free energy $F_{\rm ph}(T)$, so we can easily find the minimum free-energy volume $V(T)$ over a large number of points. We also computed the linear expansion coefficient (8) using five-point numerical differentiation of the volume.

The thermal expansion of α-Sn is shown in Figs. 23 (PBE) and 24 (SCAN), compared to data taken by Touloukian *et al.* [83]. Even though PBE overestimates the equilibrium volume, its predicted value of $\alpha(T)$ is in good agreement with experiment for low temperatures and shows the same flattening at high temperature, albeit at a higher value than found by experiment. SCAN is somewhat less accurate at low temperatures and shows a decreasing value of α above 150 K.

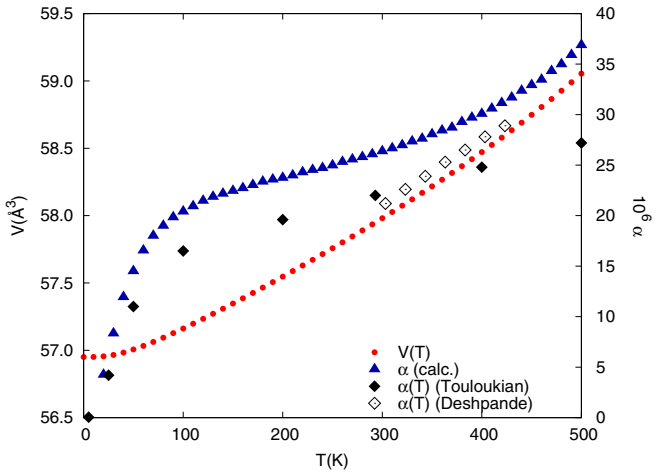

FIG. 25. The primitive-cell volume of β-Sn as a function of temperature (left axis, red circles) and the linear expansion coefficient α (right axis, blue triangles) calculated by APL using the PBE density functional. We also plot the value of α(T) found in Touloukian *et al.* [83] (solid black diamonds) and measured by Deshpande and Sirdeshmukh [77] (open black diamonds).

β-Sn has a tetragonal lattice, so the lattice parameters $a(T)$ and $c(T)$ can have different thermal expansion coefficients,

$$\alpha_{\parallel}(T) = \frac{1}{a(T)}\frac{da}{dT}(T) \quad \text{and}\, \alpha_{\perp}(T) = \frac{1}{c(T)}\frac{dc}{dT}(T), \quad (10)$$

where $\parallel$ and $\perp$ denote expansion in the a, b plane and along the c axis, respectively. The averaged thermal expansion is then

$$\alpha(T) = \tfrac{1}{3}[2\alpha_{\parallel}(T) + \alpha_{\perp}(T)]. \quad (11)$$

We compare predicted thermal expansion of β-Sn to the experimental data cited in Touloukian *et al.* [83] (solid black diamonds) and measured by Deshpande and Sirdeshmukh [77] in Figs. 25 (PBE) and 26 (SCAN). The results here are reversed from α-Sn, in that SCAN has a much better prediction for $\alpha(T)$ than PBE. Given the problems noted with β-Sn in the PBE, it is not surprising that we only get agreement between theory and experiment below 50 K. The SCAN functional is within 10% of experiment at temperatures below 300 K, but its functional form is different, flattening above 100 K, while the experimental $\alpha(T)$ continues to increase up to 500 K.

There is no experimental information about the thermal expansion of γ-Sn or even $Sn_{0.8}In_{0.2}$, but we can determine the thermal expansion parameter, which we plot in Figs. 27 (PBE) and 28 (SCAN). We find that $\alpha(T)$ is in the same range as β-Sn, but there is a very large difference in the behavior of $\alpha(T)$ in the two phases.

The results of this section are confusing. SCAN gives a much better prediction of the equilibrium lattice constants of all three phases than PBE does, but the high-temperature behavior of $\alpha(T)$ differs from experiment in all cases, and there are large differences between PBE and SCAN. More study

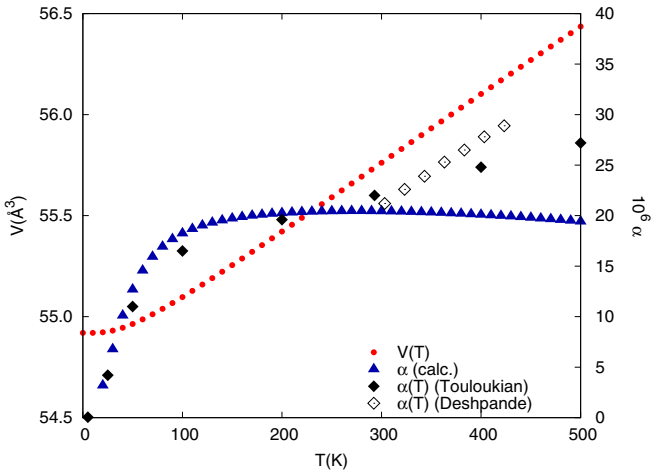

FIG. 26. The primitive-cell volume of β-Sn as a function of temperature (left axis, red circles) and the linear expansion coefficient α (right axis, blue triangles) calculated by APL using the SCAN density functional. We also plot the value of α(T) found in Touloukian *et al.* [83] (solid black diamonds) and measured by Deshpande and Sirdeshmukh [77] (open black diamonds).

is needed here, including going beyond the quasiharmonic approximation.

In general both PBE and SCAN give reasonable values of $\alpha(T)$ for $T < 100$ K, but the higher temperature behavior deviates from experiment. This may be due to the failure of the harmonic approximation or may be that we simply require a finer volume mesh to determine the equilibrium volume $V(T)$.

C. Thermal phase transitions

Having shown that APL/AFLOW/VASP finds reasonably accurate phonon spectra and gives us the correct order of magnitude of the thermal expansion parameter, we turn to the main question of this study: Can we predict the transition from α- to β-Sn, and is there a transition from β- to γ-Sn?

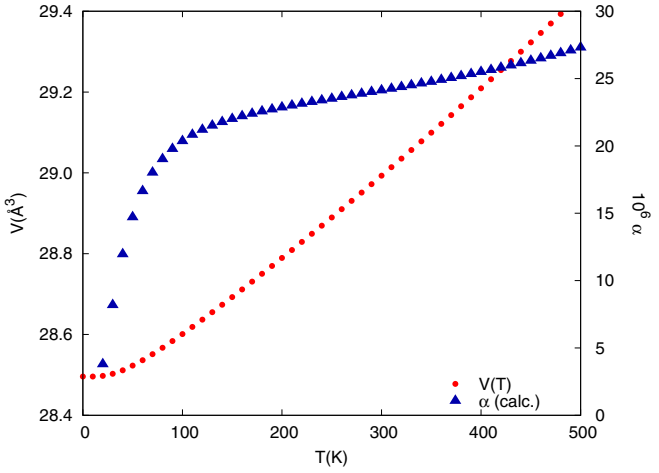

FIG. 27. The primitive-cell volume of γ-Sn as a function of temperature (left axis, red circles) and the linear expansion coefficient α (right axis, blue triangles) calculated by APL using the PBE density functional.

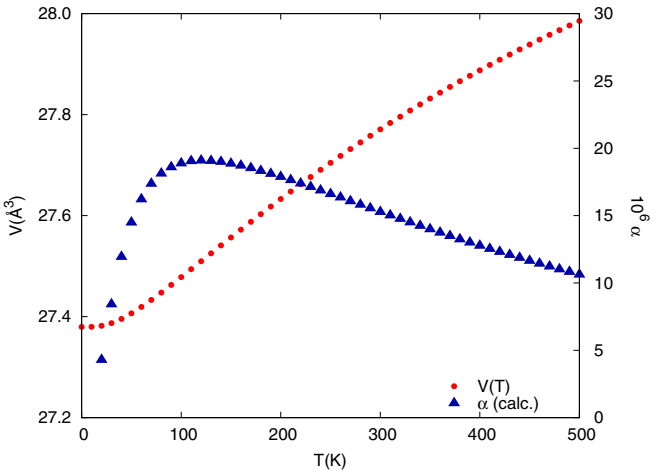

FIG. 28. The primitive-cell volume of γ-Sn as a function of temperature (left axis, red circles) and the linear expansion coefficient α (right axis, blue triangles) calculated by APL using the SCAN density functional.

We have determined the free energy $F(T)$ for all three phases using the PBE and SCAN functionals as outlined at the start of this section. Figure 29 shows the results for the PBE functional, with the free energy for all three phases plotted on the top of the graph and the deviation of the free energy from α-Sn at the bottom. The transition to γ-Sn is predicted to occur at 400 K, not too far from the 450 K transition, but it occurs before the transition to β-Sn, which would be at about 425 K.

It could be argued that we should use the larger energy cutoff and k-point mesh from Table II to do these calculations, but this will only shift the static energy of β-Sn 1 meV/atom below the γ-Sn result. By the time we get to 400 K the free energy of γ-Sn will still be lower than β-Sn.

The SCAN functional correctly predicts the ordering $U(\alpha\text{-Sn}) < U(\beta\text{-Sn}) < U(\gamma\text{-Sn})$ (Fig. 13), so perhaps it will do better, even though the static energy difference between α- and β-Sn is quite large. One complication is the low energy of the simple cubic phase, which is actually lower in energy than γ-Sn. Because of this we did a full set of phonon calculations for the simple cubic phase, using a $5 \times 5 \times 5$ (125 atom) supercell with a $4 \times 4 \times 4$ k-point mesh (18 k points in the irreducible Brillouin zone). The simple cubic phase is vibrationally unstable for volumes *below* 28 Å^3/atom, so we only consider larger volumes in computing the free energy.

The results of these calculations are shown in Fig. 30. Again, the top panel shows the free energy of four phases, and the bottom shows the deviation from α-Sn. The simple cubic free energy is such that this phase is above γ-Sn for temperatures greater than 120 K, so we can ignore it entirely. The SCAN functional predicts that β-Sn will be below γ-Sn for temperatures up to 280 K. If the free energy difference between β-Sn and α-Sn was lowered by some 40 meV/atom SCAN would predict the correct ordering of the states. Unfortunately the free energy difference is about 67 meV/atom, so SCAN predicts a transition from α-Sn to γ-Sn at about 700 K, well above the observed melting point of tin of 505 K [82]. This means that SCAN does not correctly describe the

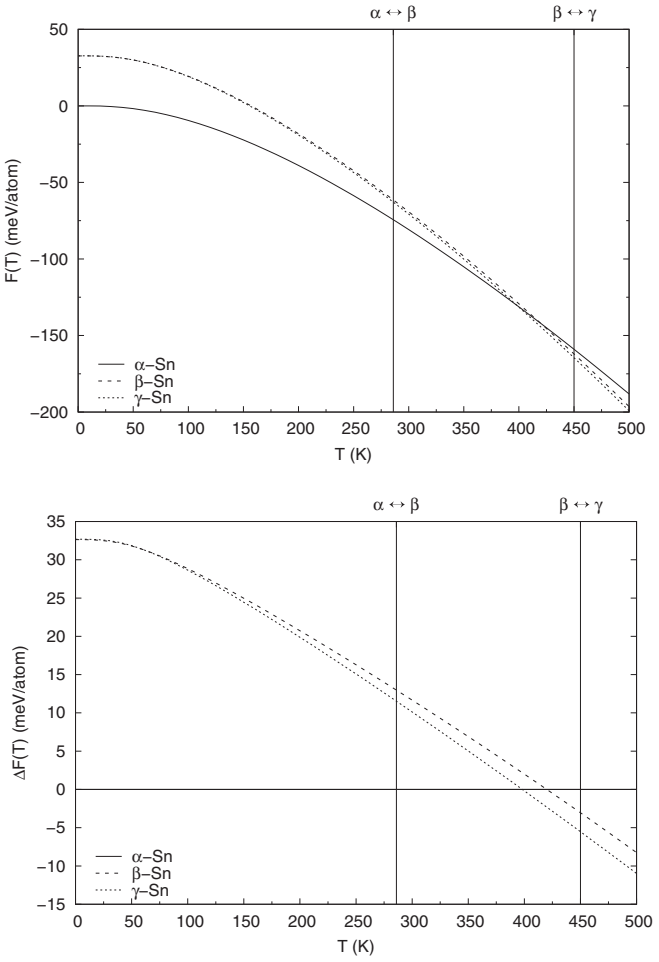

FIG. 29. Free energy predicted by the PBE functional [(6), (7)] as a function of temperature for α-Sn (solid line), β-Sn (dashed line), and simple hexagonal γ-Sn (dotted line). The vertical lines show the experimental α-β phase transition at 286 K [10] and β-γ transition at 450 K [12]. Top: the free energy of each phase shifted so that the energy of the α phase is zero at $T = 0$. Bottom: the difference in energy of the β and γ phases with respect to α-Sn.

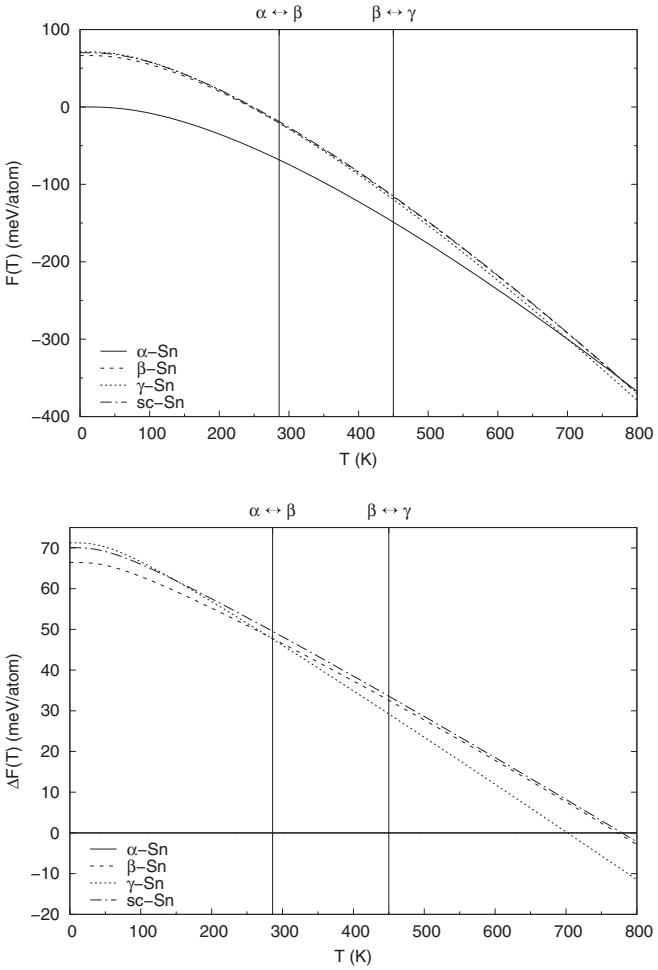

FIG. 30. Free energy predicted by the SCAN functional [(6), (7)] as a function of temperature for α-Sn (solid line), β-Sn (dashed line), simple hexagonal γ-Sn (dotted line), and simple cubic tin (dash-dot line). The vertical lines show the experimental α-β phase transitions at 286 K [10] and 450 K [12]. Top: the free energy of each phase shifted so that the energy of the α phase is zero at $T = 0$. Bottom: the difference in energy of the β- and γ-, and simple cubic phases with respect to α-Sn.

physics of tin, but since it predicts a reasonable temperature for the β-γ transition perhaps we can say that it is better than the PBE functional.

IX. ELECTRONIC CONTRIBUTIONS TO THE FREE ENERGY

The preceding calculations neglect the thermal energy of the electrons. One can argue that this must be small compared to the vibrational energy, since the electronic contributions to metallic specific heats are much smaller than the vibrational contributions [84]. In this case, however, the energy differences between the tin phases are themselves small, so it is possible that the relatively small electron energy may be large enough to change the ordering among phases.

The Kohn-Sham electronic eigenvalues found in DFT calculations represent an independent approximation to the true electron energies in the system. Using these eigenvalues, the free energy of a system with electronic density of states $\rho(\varepsilon)$ is [85]

$$U_{\rm elec}(T) = \int d\varepsilon\, \varepsilon\, \rho(\varepsilon) f(\varepsilon, T), \tag{12}$$

where

$$f(\varepsilon, T) = \frac{1}{e^{\beta[\varepsilon - \mu(T)]} + 1} \tag{13}$$

is the Fermi distribution function, and the chemical potential $\mu(T)$ is chosen so that

$$N_{\rm elec} = \int d\varepsilon\, \rho(\varepsilon) f(\varepsilon, T). \tag{14}$$

Here $N_{\rm elec}$ is the number of valence electrons in the system, four per atom for tin. The entropy of this distribution of

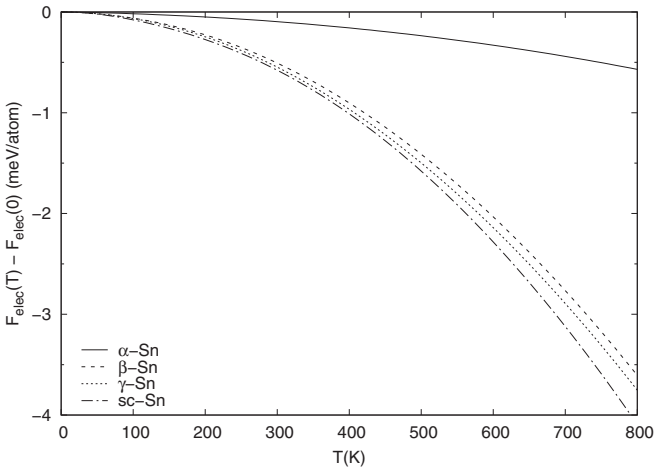

FIG. 31. The approximate contribution (16) electrons to the free energy of α-Sn (solid line), β-Sn (dashed line), γ-Sn (dotted line), and simple cubic tin (dash-dot line) at the equilibrium volume of each phase using the SCAN functional.

electrons is

$$S_{\rm elec}(T) = -k \int d\varepsilon\, \rho(\varepsilon) \begin{Bmatrix} f(\varepsilon,T)\ln f(\varepsilon,T) + \\ [1-f(\varepsilon,T)]\ln[1-f(\varepsilon,T)] \end{Bmatrix}, \tag{15}$$

and the resulting contribution to the free energy of the system is

$$F_{\rm elec}(T) = U_{\rm elec}(T) - TS_{\rm elec}(T). \tag{16}$$

We can compute (16) using the eigenvalues and density of states found by VASP. Here we only present an example, the free energy of the α, β, γ and simple cubic tin phases at equilibrium using the SCAN functional (see Fig. 12). The results are shown in Fig. 31. The zero-temperature contribution of the electrons to the total energy are included in the ground-state calculation, so we are only interested in the thermal contribution to the free energy, $F_{\rm elec}(T) - F_{\rm elec}(0)$. We see that the electronic contribution is indeed small compared to the free energy shown in Fig. 30. The electronic free energy of the metallic phases changes by about 4 meV/atom from 0–800 K, compared to the 400 meV/atom change of the original free energy. The change in the electronic free energy of semimetallic α-Sn is no more than 0.5 meV/atom in this range.

This is not to say that the electronic free energy cannot influence the predictions of transition temperatures. The difference between α- and γ-Sn is about 3 meV/atom at 700 K. This will drive the α-γ transition temperature down by about 50 K. Unfortunately $F_{\rm elec}$ for β-Sn is above that of γ-Sn, hence the electrons will not help to move the β-Sn free energy below γ-Sn, and there is still no α-β transition predicted by SCAN. Indeed, the difference between the simple cubic and β-Sn electronic free energies is such that if we add the electronic free energy to the results of Fig. 30 the two phases will be essentially degenerate, contrary to experiment.

In general the electronic contribution to the free energy is small compared to the vibrational contribution, but it is large enough to change the structural transition temperature by about 10%. It is not, however, large enough to change our conclusion that no functional correctly predicts the thermal transition sequence in tin.

The caveat here is that we do not have the true electronic spectra of tin. We only have the Kohn-Sham independent electron eigenvalues, which are known to be at best only an approximation to the true electronic excitation spectra [86]. At best, then, we can only use our Kohn-Sham eigenvalues to estimate the electronic contribution to the free energy. Although this should not significantly change the results we cannot conclusively prove this.

X. DISCUSSION

As noted in the introduction, this work is only concerned with the quasiharmonic approximation to the vibrational properties of tin, with volume-dependent harmonic interatomic force constants for each structure. Some experimental studies of anharmonicity have been done on both α-Sn [87] and β-Sn [88], with the latter saying "the anharmonic effect in white tin is weak." At some point the QHA must fail, as tin melts at 505 K, not far from the observed β-γ transition. Calculation of the melting temperature would involve a molecular dynamics calculation, and that is far beyond the scope of this paper.

It is doubtful that anharmonicity would introduce large enough corrections to help the predictions for the non-SCAN metaGGAs, as this would involve extremely large changes in the free energy for some phases, on the order of 100 meV/atom. Even the GGA AM05 structure would require that β- and γ-Sn have anharmonic corrections that are around 30 meV/atom different than that found for α-Sn. This too seems unlikely.

Returning to the QHA calculations of this paper, we find that most of the functionals studied predict β-Sn to be the ground state, contrary to experiment. The empirical metaGGA functionals actually predict a close-packed ground state for tin. Only the PBE and SCAN functionals give the correct ground state, α-Sn, and only SCAN unambiguously places equilibrium γ-Sn above β-Sn.

The purpose of this study is twofold: first, to see if high-throughput methods, in particular AFLOW, could accurately describe the system using their default settings and second, to see if DFT can adequately describe the thermodynamic behavior of tin.

The first question can be answered "yes." The results in Table II show that the static energy calculations are sufficiently converged for our purposes, and the phonon convergence tests in Sec. VII show that the vibrational free energy of the system is insensitive to the supercell size. It should be stressed that the last point is a result of the averaging over the phonon density of states in both the zero-point and vibrational contributions to the free energy (5). The phonon spectra themselves show differences, in some cases rather large, between calculations using different cell sizes, and between calculation and experiment, however these differences are minimized because of the averaging effect of the integrals over the phonon density of states.

While neither PBE nor SCAN correctly predict the behavior of tin, we can say that they describe the trend of the vibrational free energy correctly. Differentiating $F(T)$ (5) with respect to temperature shows that $F'(T) < 0$ for all

temperatures. To see the observed phase transitions in tin, at zero temperature we must have the ordering $\alpha < \beta < \gamma$, but the free energy of β-Sn must fall off faster than that of α-Sn, and the free energy of γ-Sn must fall off faster than the other two. This is the case for both PBE and SCAN. The reason for this can be seen in Fig. 22. The phonon density of states for α-Sn is dominated by the peak in the optical modes near 6 THz, well beyond the maximum vibrational frequency of the other two phases. β-Sn has a large peak in its optical modes near 4 THz, where the pDOS of γ-Sn is much less pronounced. Since the thermal part of the free energy integral (5) is weighted toward lower phonon energies, it follows that these phonon spectra will give the correct ordering.

Although the electronic contribution to the thermal free energy is small, our independent electron estimate of its impact shows that it can change the phase transition temperature and may even change the ordering of the nearly degenerate β-Sn and simple cubic Sn phases found by the SCAN functional. It does not, however, change our fundamental conclusion that none of the density functionals correctly predict the correct tin phase transition sequence.

If we are required to say which of these functionals gives the "best" description of tin, albeit still incorrect, it is our opinion that the SCAN functional is the winner. Not only does SCAN give better ground state densities than PBE, it also gives the β-Sn $\rightarrow$ γ-Sn transition at a reasonable temperature, even if it predicts that it cannot be observed. However, it is obvious from this study that we still need better density functionals to adequately describe the behavior of tin.

In conclusion, we have shown that high-throughput calculations can be used to determine the thermal behavior of tin as for any given density functional. Unfortunately all of the currently available functionals are flawed, with SCAN being better than the others, although it does not predict the correct ordering of the phase transitions in tin. Fortunately we now have a platform to quickly evaluate new density functionals as they become available.

ACKNOWLEDGMENTS

An anonymous referee suggested we consider the electronic contribution to the free energy, which led to the discussion in Sec. IX. The authors thank Ohad Levy and Cormac Toher for valuable discussions. This work has been supported by ONR Grant No. N00014-20-1-2525. R.F. acknowledges support from the Alexander von Humboldt foundation under the Feodor Lynen research fellowship. Some calculations were performed using the United States Naval Academy's Cray computer, Grace.

[1] P. L. Couteur and J. Burreson, *Napoleon's Buttons: How 17 Molecules Changed History* (Tarcher Perigee, New York, 2004).
[2] R. C. Lasky, Tin Pest: Elusive Threat in Lead-Free Soldering? J Fail. Anal. and Preven. **10**, 437 (2010).
[3] J. Fritzsche, Ueber eigenthülich modificirtes Zinn, Ber. Dtsch. Chem. Ges. **2**, 112 (1869).
[4] K. Schaum, Ueber hylotrop-isomere Körperformen, Justus Liebigs Annal. Chem. **308**, 18 (1899).
[5] N. D. Burns, A Tin Pest Failure, J Fail. Anal. and Preven. **9**, 461 (2009).
[6] W. J. Plumbridge, Tin pest issues in lead-free electronic solders, J. Mater. Sci.: Mater. Electron. **18**, 307 (2007).
[7] R. Pfister and P. Pugnat, *Tin Pest: A Forgotten Issue in the Field of Applied Superconductivity?* arXiv:1204.1443.
[8] B. Cornelius, S. Treivish, Y. Rosenthal, and M. Pecht, The phenomenon of tin pest: A review, Microelectron. Reliab. **79**, 175 (2017).
[9] J. Donohue, *The Structure of the Elements* (John Wiley & Sons, Inc., New York, 1974).
[10] E. Cohen and A. K. W. A. van Lieshout, Physikalisch-chemische Stadien am Zinn. X. Die Umwandlungstemperatur graues Zinn $\rightleftharpoons$ weisses Zinn, Z. Phys. Chem. **173**, 32 (1935).
[11] Grey Tin (Tin Pest) Time-Lapse Video, https://youtube/FUoVEmHuykM.
[12] R. Kubiak, Evidence for the existence of the γ form of tin, J. Less-Common Met. **116**, 307 (1986).
[13] R. H. Kane, B. C. Giessen, and N. J. Grant, New metastable phases in binary tin alloy systems, Acta Metall. **14**, 605 (1966).
[14] A. S. Ivanov, A. Y. Rumiantsev, B. Dorner, N. L. Mitrofanov, and V. V. Pushkarev, Lattice dynamics and electron-phonon interaction in γ-tin, J. Phys. F: Met. Phys. **17**, 1925 (1987).
[15] A. S. Ivanov, A. Y. Rumiantsev, N. L. Mitrofanov, and M. Alba, Low-frequency lattice dynamics of γ-tin, Physica B **174**, 79 (1974).
[16] E. Parthé, L. Gelato, B. Chabot, M. Penso, K. Cenzula, and R. Gladyshevskii, Standardized Data and Crystal Chemical Characterization of Inorganic Structure Types, *Gmelin Handbook of Inorganic and Organometallic Chemistry*, 8th ed. (Springer-Verlag, Berlin, Heidelberg, 1993), Vol. 2.
[17] P. Pavone, S. Baroni, and S. de Gironcoli, $\alpha \leftrightarrow \beta$ phase transition in tin: A theoretical study based on density-functional perturbation theory, Phys. Rev. B **57**, 10421 (1998).
[18] K. Houben, J. K. Jochum, D. P. Lozano, M. Bisht, E. Menéndez, D. G. Merkel, R. Rüffer, A. I. Chumakov, S. Roelants, B. Partoens, M. V. Milošević, F. M. Peeters, S. Couet, A. Vantomme, K. Temst, and M. J. V. Bael, *In situ* study of the α-Sn to β-Sn phase transition in low-dimensional systems: Phonon behavior and thermodynamic properties, Phys. Rev. B **100**, 075408 (2019).
[19] J. Ihm and M. L. Cohen, Equilibrium properties and the phase transition of grey and white tin, Phys. Rev. B **23**, 1576 (1981).
[20] S.-H. Na and C.-H. Park, First-principles study of the structural phase transition in Sn, J. Korean Phys. Soc. **56**, 494 (2010).
[21] F. Legrain, O. I. Malyi, C. Persson, and S. Manzhos, Comparison of alpha and beta tin for lithium, sodium, and magnesium storage: An *ab initio* study including phonon contributions, J. Chem. Phys. **143**, 204704 (2015).
[22] F. Legrain and S. Manzhos, Understanding the difference in cohesive energies between alpha and beta tin in DFT calculations, AIP Adv. **6**, 045116 (2016).
[23] S. Curtarolo, W. Setyawan, G. L. W. Hart, M. Jahnátek, R. V. Chepulskii, R. H. Taylor, S. Wang, J. Xue, K. Yang, O. Levy,

M. J. Mehl, H. T. Stokes, D. O. Demchenko, and D. Morgan, AFLOW: An automatic framework for high-throughput materials discovery, Comput. Mater. Sci. **58**, 218 (2012).

[24] C. Toher, C. Oses, D. Hicks, E. Gossett, F. Rose, P. Nath, D. Usanmaz, D. C. Ford, E. Perim, C. E. Calderon, J. J. Plata, Y. Lederer, M. Jahnátek, W. Setyawan, S. Wang, J. Xue, K. Rasch, R. V. Chepulskii, R. H. Taylor, G. Gomez, H. Shi *et al.*, *The AFLOW Fleet for Materials Discovery*, in *Handbook of Materials Modeling*, edited by W. Andreoni and S. Yip (Springer International Publishing, Cham, Switzerland, 2018), pp. 1–28.

[25] C. Oses, C. Toher, and S. Curtarolo, Data-driven design of inorganic materials with the Automatic Flow Framework for Materials Discovery, MRS Bull. **43**, 670 (2018).

[26] C. Nyshadham, C. Oses, J. E. Hansen, I. Takeuchi, S. Curtarolo, and G. L. W. Hart, A computational high-throughput search for new ternary superalloys, Acta Mater. **122**, 438 (2017).

[27] M. Jahnátek, O. Levy, G. L. W. Hart, L. J. Nelson, R. V. Chepulskii, J. Xue, and S. Curtarolo, Ordered phases in ruthenium binary alloys from high-throughput first-principles calculations, Phys. Rev. B **84**, 214110 (2011).

[28] Y. Lederer, C. Toher, K. S. Vecchio, and S. Curtarolo, The search for high entropy alloys: A high-throughput *ab-initio* approach, Acta Mater. **159**, 364 (2018).

[29] J. J. Plata, P. Nath, D. Usanmaz, J. Carrete, C. Toher, M. de Jong, M. D. Asta, M. Fornari, M. Buongiorno Nardelli, and S. Curtarolo, An efficient and accurate framework for calculating lattice thermal conductivity of solids: AFLOW-AAPL Automatic Anharmonic Phonon Library, npj Comput. Mater. **3**, 45 (2017).

[30] G. Kresse and J. Hafner, Ab initio molecular dynamics for liquid metals, Phys. Rev. B **47**, 558 (1993).

[31] G. Kresse and J. Hafner, *Ab initio* molecular-dynamics simulation of the liquid-metal-amorphous-semiconductor transition in germanium, Phys. Rev. B **49**, 14251 (1994).

[32] G. Kresse and J. Furthmüller, Efficiency of *ab-initio* total energy calculations for metals and semiconductors using a plane-wave basis set, Comput. Mater. Sci. **6**, 15 (1996).

[33] G. Kresse and J. Furthmüller, Efficient iterative schemes for *ab initio* total-energy calculations using a plane-wave basis set, Phys. Rev. B **54**, 11169 (1996).

[34] M. J. Mehl, D. Finkenstadt, C. Dane, G. L. W. Hart, and S. Curtarolo, Finding the stable structures of $N_{1-x}W_x$ with an *ab initio* high-throughput approach, Phys. Rev. B **91**, 184110 (2015).

[35] P. Carrier, R. Wentzcovitch, and J. Tsuchiya, First-principles prediction of crystal structures at high temperatures using the quasiharmonic approximation, Phys. Rev. B **76**, 064116 (2007).

[36] M. J. Mehl, D. Hicks, C. Toher, O. Levy, R. M. Hanson, G. Hart, and S. Curtarolo, The AFLOW Library of Crystallographic Prototypes: Part 1, Comput. Mater. Sci. **136**, S1 (2017).

[37] D. Hicks, M. J. Mehl, E. Gossett, C. Toher, O. Levy, R. M. Hanson, G. Hart, and S. Curtarolo, The AFLOW Library of Crystallographic Prototypes: Part 2, Comput. Mater. Sci. **161**, S1 (2019).

[38] D. Hicks, M. J. Mehl, M. Esters, C. Oses, O. Levy, G. L. W. Hart, C. Toher, and S. Curtarolo, *The AFLOW Library of Crystallographic Prototypes: Part 3*, arXiv:2012.05961 (Comput. Mater. Sci. to be published).

[39] P. P. Ewald, C. Hermann, O. Lohrmann, H. Philipp, C. Gottfried, F. Schossberger, and K. Herrmann, eds., *Strukturbericht* (Akademische Verlagsgesellschaft M. B. H., 1937-1943), Vol. I–VII.

[40] C. J. Smithells, *Metals Reference Book* (Butterworths Scientific, London, 1955), 2nd ed.

[41] A. Yoshiasa, Y. Murai, O. Ohtaka, and T. Katsura, Detailed Structures of Hexagonal Diamond (lonsdaleite) and Wurtzite-type BN, Jpn. J. Appl. Phys. **42**, 1694 (2003).

[42] Available online at http://www.aflow.org/prototype-encyclopedia.

[43] G. V. Raynor and J. A. Lee, The tin-rich intermediate phases in the alloys of tin with cadmium, indium and mercury, Acta Metall. **2**, 616 (1954).

[44] R. J. Needs and R. M. Martin, Transition from β-Sn to simple hexagonal silicon under pressure, Phys. Rev. B **30**, 5390 (1984).

[45] G. J. Ackland, High-pressure phases of group IV and III-V semiconductors, Rep. Prog. Phys. **64**, 483 (2001).

[46] E. C. Bain and N. V. Dunkirk, The nature of martensite, Trans. AIME **70**, 25 (1924).

[47] B. Wehinger, A. Bosak, G. Piccolboni, K. Refson, D. Chernyshov, A. Ivanov, A. Rumiantsev, and M. Krisch, Diffuse scattering in metallic tin polymorphs, J. Phys.: Condens. Matter **26**, 115401 (2014).

[48] N. G. Hörmann, A. Gross, J. Rohrer, and P. Kaghazchi, Stabilization of the γ-Sn phase in tin nanoparticles and nanowires, Appl. Phys. Lett. **107**, 123101 (2015).

[49] L. Hedin and B. I. Lundqvist, Explicit local exchange-correlation potentials, J. Phys. C: Solid State Phys. **4**, 2064 (1971).

[50] D. M. Ceperley and B. J. Alder, Ground State of the Electron Gas by a Stochastic Method, Phys. Rev. Lett. **45**, 566 (1980).

[51] J. P. Perdew and A. Zunger, Self-interaction correction to density-functional approximations for many-electron systems, Phys. Rev. B **23**, 5048 (1981).

[52] W. Kohn and L. J. Sham, Self-Consistent Equations Including Exchange and Correlation Effects, Phys. Rev. **140**, A1133 (1965).

[53] J. P. Perdew, K. Burke, and M. Ernzerhof, Generalized Gradient Approximation Made Simple, Phys. Rev. Lett. **77**, 3865 (1996).

[54] J. P. Perdew, A. Ruzsinszky, G. I. Csonka, O. A. Vydrov, G. E. Scuseria, L. A. Constantin, X. Zhou, and K. Burke, Restoring the Density-Gradient Expansion for Exchange in Solids and Surfaces, Phys. Rev. Lett. **100**, 136406 (2008).

[55] R. Armiento and A. E. Mattsson, Functional designed to include surface effects in self-consistent density functional theory, Phys. Rev. B **72**, 085108 (2005).

[56] A. E. Mattsson, R. Armiento, J. Paier, G. Kresse, J. M. Wills, and T. R. Mattsson, The AM05 density functional applied to solids, J. Chem. Phys. **128**, 084714 (2008).

[57] J. Tao, J. P. Perdew, V. N. Staroverov, and G. E. Scuseria, Climbing the Density Functional Ladder: Nonempirical Meta-Generalized Gradient Approximation Designed for Molecules and Solids, Phys. Rev. Lett. **91**, 146401 (2003).

[58] J. P. Perdew, A. Ruzsinszky, G. I. Csonka, L. A. Constantin, and J. Sun, Workhorse Semilocal Density Functional for Condensed Matter Physics and Quantum Chemistry, Phys. Rev. Lett. **103**, 026403 (2009).

[59] J. Sun, B. Xiao, and A. Ruzsinszky, Communication: Effect of the orbital-overlap dependence in the meta generalized gradient approximation, J. Chem. Phys. **137**, 051101 (2012).

[60] J. Sun, R. Haunschild, B. Xiao, I. W. Bulik, G. E. Scuseria, and J. P. Perdew, Semilocal and hybrid meta-generalized gradient approximations based on the understanding of the kinetic-energy-density dependence, J. Chem. Phys. **138**, 044113 (2013).

[61] Y. Zhao and D. G. Truhlar, A new local density functional for main-group thermochemistry, transition metal bonding, thermochemical kinetics, and noncovalent interactions, J. Chem. Phys. **125**, 194101 (2006).

[62] J. Sun, A. Ruzsinszky, and J. Perdew, Strongly Constrained and Appropriately Normed Semilocal Density Functional, Phys. Rev. Lett. **115**, 036402 (2015).

[63] J. Sun, R. C. Remsing, Y. Zhang, Z. Sun, A. Ruzsinszky, H. Peng, Z. Yang, A. Paul, U. Waghmare, X. Wu, M. L. Klein, and J. P. Perdew, Accurate first-principles structures and energies of diversely bonded systems from an efficient density functional, Nat. Chem. **8**, 831 (2016).

[64] G. I. Csonka, J. P. Perdew, A. Ruzsinszky, P. H. T. Philipsen, S. Lebègue, J. Paier, O. A. Vydrov, and J. G. Ángyán, Assessing the performance of recent density functionals for bulk solids, Phys. Rev. B **79**, 155107 (2009).

[65] J. Sun, M. Marsman, G. I. Csonka, A. Ruzsinszky, P. Hao, Y.-S. Kim, G. Kresse, and J. P. Perdew, Self-consistent meta-generalized gradient approximation within the projector-augmented-wave method, Phys. Rev. B **84**, 035117 (2011).

[66] P. E. Blöchl, Projector augmented-wave method, Phys. Rev. B **50**, 17953 (1994).

[67] G. Kresse and D. Joubert, From ultrasoft pseudopotentials to the projector augmented-wave method, Phys. Rev. B **59**, 1758 (1999).

[68] E. M. Lifshitz and L. P. Pitaevskii, *Statistical Physics Part 1* (Pergamon Press, Oxford, New York, Toronto, Sydney, Paris, Frankfurt, 1980), *Landau and Lifshitz Course of Theoretical Physics*, 3rd ed, Vol. 5, Chap. 6, p. 193.

[69] F. Birch, Finite strain isotherm and velocities for single-crystal and polycrystalline NaCl at high pressures and 300 °K, J. Geophys. Res. **83**, 1257 (1978).

[70] M. J. Mehl, Pressure dependence of the elastic moduli in aluminum-rich Al-Li compounds, Phys. Rev. B **47**, 2493 (1993).

[71] R. M. Hanson, J. Prilusky, Z. Renjian, T. Nakane, and J. L. Sussman, *Jmol*. An open-source Java viewer for chemical structures in 3D.

[72] M. Mitchell, *Engauge Digitizer* (2019), open source software, version 12.

[73] C. E. Calderon, J. J. Plata, C. Toher, C. Oses, O. Levy, M. Fornari, A. Natan, M. J. Mehl, G. Hart, M. B. Nardelli, and S. Curtarolo, The {AFLOW} standard for high-throughput materials science calculations, Comput. Mater. Sci. **108, Part A**, 233 (2015).

[74] D. L. Price, J. M. Rowe, and R. M. Nicklow, Lattice Dynamics of Grey Tin and Indium Antimonide, Phys. Rev. B **3**, 1268 (1971).

[75] J. M. Rowe, B. N. Brockhouse, and E. C. Svensson, Lattice Dynamics of White Tin, Phys. Rev. Lett. **14**, 554 (1965).

[76] D. L. Price, Lattice Dynamics of White Tin, Proc. R. Soc. Series A Math. Phys. Sci. **300**, 25 (1967).

[77] V. T. Deshpande and D. B. Sirdeshmukh, Thermal Expansion of Tetragonal Tin, Acta Cryst. **14**, 355 (1961).

[78] N. E. Christensen and M. Methfessel, Density-functional calculations of the structural properties of tin under pressure, Phys. Rev. B **48**, 5797 (1993).

[79] H. Olijnyk and W. B. Holzapfel, Phase Transitions in Si, Ge and Sn under Pressure, J. Phys. Colloques **45**, 153 (1984).

[80] W. Setyawan and S. Curtarolo, High-throughput electronic band structure calculations: Challenges and tools, Comput. Mater. Sci. **49**, 299 (2010).

[81] M. Aouissi, I. Hamdi, N. Meskini, and A. Qteish, Phonon spectra of diamond, Si, Ge, and α-Sn: Calculations with real-space interatomic force constants, Phys. Rev. B **74**, 054302 (2006).

[82] C. J. Smithells, *Metals Reference Book* (Butterworths Scientific, London, 1949).

[83] Y. S. Touloukian, R. K. Kirby, R. E. Taylor, and P. D. Desai, *Thermal Expansion Metallic Elements and Alloys*, Thermophysical Properties of Matter - The TPRC Data Series (IFI/Plenum, New York, 1975), Vol. 12, pp. 339–345.

[84] N. W. Ashcroft and N. D. Mermin, *Solid State Physics*, college ed (Harcourt Brace College Publishers, Fort Worth, 1976), Chap. 23, pp. 463–464.

[85] N. W. Ashcroft and N. D. Mermin, *Solid State Physics*, college ed. (Harcourt Brace College Publishers, Fort Worth, 1976), Chap. 2, pp. 40–55.

[86] L. J. Sham and M. Schlüter, Density-Functional Theory of the Energy Gap, Phys. Rev. Lett. **51**, 1888 (1983).

[87] D. H. Bilderback and R. Colella, Valence charge density in grey tin: X-ray determination of the (222) "forbidden" reflection and its temperature dependence, Phys. Rev. B **11**, 793 (1975).

[88] M. Merisalo and M. Järvinen, Anharmonicity of lattice vibrations in white tin by X-ray measurement of almost-forbidden reflections, Phil. Mag. B **37**, 233 (1978).